Generation of vortex electrons in tunneling ionization of polyatomic molecules: Exact results in the zero-range potential model

Kirill V. Bazarov [1,2,*] and Oleg I. Tolstikhin [1,†]

[1]*Moscow Institute of Physics and Technology*, *Dolgoprudny 141700, Russia*
[2]*NRC "Kurchatov Institute", Moscow 123182, Russia*

The theory of molecular Siegert states in a static electric field in the zero-range potential model is developed. The model admits extended analytical and accurate numerical treatments, which enables one to study tunneling ionization of large polyatomic molecules with complex geometry in strong fields beyond the weak-field approximation. The theory is illustrated by calculations for three model molecules reproducing the geometry of the real water, benzene, and leucine molecules. The field and orientation dependence of two major ionization observables, the ionization rate and the transverse momentum distribution of liberated electrons, is analyzed. The calculations reveal a number of strong-field effects not accounted for by the weak-field asymptotic theory. In particular, it is shown that vortex electrons are efficiently generated in tunneling ionization of large molecules at sufficiently strong fields, which opens a perspective for enantiosensitive rescattering photoelectron spectroscopy. The mechanism of tunneling-induced electron diffraction and its manifestation in the transverse momentum distribution are discussed.

I. INTRODUCTION

Tunneling ionization is the first step for a variety of processes in strong-field physics [1]. In the adiabatic regime ionization in a time-dependent laser field proceeds as if the field were static and equal to the instantaneous laser field [2]. In view of numerous applications in strong-field physics, the theory of tunneling ionization of molecules in a static electric field continues to attract much interest.

The key ionization observable needed for applications is the ionization rate as a function of the ionizing field strength F and the orientation of the molecule with respect to the field. Without attempting to comprehensively review the literature, we indicate three approaches to accurately calculate ionization rates of molecules at different levels of approximation. The simplest is an approach based on the single-active-electron approximation (SAEA) in which only one electron bound by a given potential modeling the parent molecular ion is treated [3–9]. The major drawback of this approach is the neglect of core polarization effects. In a more involved antisymmetrized coupled channels approach the multielectron molecular wave function is composed of Gaussian orbitals for bound electrons and finite-element basis functions for the liberated electron [10]. An important achievement of this approach is the demonstration that in some cases, particularly for the CO molecule, accounting for core polarization is essential for obtaining correct orientation dependence of the ionization rate. Finally, there exists an *ab initio* coupled-cluster method with complex-scaled basis functions capable

of producing converged fully correlated results [11]. Calculations by this method for few-atomic molecules CO, O_2, H_2O, and CH_4 revealed the importance of taking into account electronic correlations. With some simplifications, the ability of the method to treat polyatomic molecules was demonstrated by calculations for benzene and naphthalene [12] and several polyacenes [13]. Although the usefulness of such computational approaches as a source of reliable results is difficult to overestimate, the calculations for polyatomic molecules are very laborious and feasible for only a few field strengths and molecular orientations.

The weak-field asymptotic theory (WFAT) of tunneling ionization of one-electron [14] and many-electron [15] systems based on the asymptotic expansion of the ionization observables in F presents an attractive alternative to computational approaches. Within the WFAT, the ionization rate and other observables needed for applications in strong-field physics are expressed analytically in terms of properties of the electronic state of the unperturbed system. Several general implementations of the WFAT for arbitrary molecules on the basis of different molecular electronic structure codes are available [16–18]. The feasibility of WFAT calculations of the orientation dependence of the ionization rate of polyatomic molecules was demonstrated, e.g., by a theoretical analysis of torsional effects in strong-field ionization of biphenyl [19] and a recent joint experimental and theoretical study on high-harmonic spectroscopy of 1,3-cyclohexadiene and benzene [20]. However, the applicability of the WFAT is limited to relatively weak fields corresponding to deep tunneling regime.

In this paper, we treat molecules in the SAEA using the zero-range potential (ZRP) model [21,22]. On the one hand, the ZRP model is not only computationally more tractable than realistic molecular potentials [4,5,8,9], but also admits

_____
*Contact author: bazarov.kv@phystech.edu
†Contact author: tolstikhin.oi@mipt.ru

an extended analytical treatment. This makes virtually exact calculations for polyatomic molecules with arbitrary geometry and orientation feasible. On the other hand, this model allows one to analyze tunneling ionization of molecules in strong fields beyond the WFAT [14]. So far, the model was used to study tunneling ionization in a static electric field from one ZRP [23], two identical [24] and different [25] ZRPs modeling atoms, homonuclear and heteronuclear diatomics, respectively. It is widely used in strong-field physics for the analysis of both strong-field ionization and high-order harmonic generation processes [26–41] (see also review articles [42,43]).

We employ the ZRP model to investigate the effect of molecular size and geometry on the ionization observables. More specifically, we are interested in the generation of vortex electrons in tunneling ionization of large molecules in strong fields. Recently, a theory of generation and rescattering of vortex photoelectrons in strong-field ionization by intense laser pulses based on the adiabatic theory [2] has been developed [44,45]. The results show that extending rescattering photoelectron spectroscopy [46–53] to vortex electrons will open a new window for molecular structure imaging in strong-field physics. In Refs. [44,45] a specific configuration was considered in which ionization occurs from a vortex bound orbital in an atom or a linear molecule aligned along the laser polarization axis having a nonzero projection of the electron angular momentum on this axis. One of the goals of this study is to demonstrate that vortex electrons are efficiently generated in tunneling ionization of large polyatomic molecules without any symmetry at sufficiently strong fields.

The paper is organized as follows. Section II summarizes basic equations of the model. Section III introduces the outgoing-wave Green's function for an electron in a homogeneous static electric field which is essential for this study. Section IV outlines a procedure to accurately calculate ionization observables in the ZRP model. The weak-field asymptotics of the observables is discussed in Sec. V. Results of illustrative calculations for three model molecules reproducing the geometry of the real water, benzene, and leucine molecules and their discussion are presented in Sec. VI. Section VII concludes the paper.

II. BASIC EQUATIONS

We consider a molecule treated in the SAEA interacting with an external static electric field. The interaction of an active electron with the molecular ion is described by a potential $V(\mathbf{r})$. The field $\mathbf{F} = F\mathbf{e}_z$, $F \geqslant 0$, is assumed to be directed along the z axis of the laboratory coordinate frame. It causes ionization of the molecule. All the ionization observables can be expressed in terms of Siegert states (SSs) in an electric field [3–5,14] which are solutions to the stationary Schrödinger equation (atomic units $\hbar = m = |e| = 1$ are used throughout)

$$\left[-\frac{1}{2}\Delta + V(\mathbf{r}) + Fz - E \right] \phi(\mathbf{r}) = 0 \tag{1}$$

satisfying the outgoing-wave boundary condition

$$\phi(\mathbf{r})|_{z \to -\infty} = \int A(\mathbf{k}_\perp) e^{i\mathbf{k}_\perp \mathbf{r}_\perp} g(z, k_\perp) \frac{d\mathbf{k}_\perp}{(2\pi)^2}, \tag{2}$$

where

$$g(z, k_\perp) = \frac{1}{|2Fz|^{1/4}} \exp\left[\frac{iF^{1/2}|2z|^{3/2}}{3} - \frac{i(k_\perp^2 - 2E)|z|^{1/2}}{(2F)^{1/2}} \right]. \tag{3}$$

Here and in the following, the subscript $\perp$ denotes the component of a vector perpendicular to the z axis. Equations (2) and (3) describe the outgoing flux of electrons liberated from the molecule by the field, with $A(\mathbf{k}_\perp)$ giving the amplitude of the transverse momentum distribution (TMD) in the flux. Equation (1) supplemented by the boundary condition (2) constitute an eigenvalue problem, and the SSs are the solutions to this problem. These states depend on the field strength F as a parameter, but we omit this dependence in the notation. Let in the absence of the field the system has a bound state with energy E_0 and real normalized wave function $\phi_0(\mathbf{r})$ satisfying Eq. (1) with $F = 0$. This state models the unperturbed ionizing molecular orbital. We are interested in the SS which originates from this bound state as the field is turned on, that is, in the solution to Eq. (1) satisfying

$$E|_{F \to 0} = E_0, \quad \phi(\mathbf{r})|_{F \to 0} = \phi_0(\mathbf{r}). \tag{4}$$

The SS eigenvalue presented in the form

$$E = \mathcal{E} - \frac{i}{2}\Gamma \tag{5}$$

defines the field-shifted energy $\mathcal{E}$ and ionization rate Γ of the state. The SS eigenfunction normalized by

$$\int \phi^2(\mathbf{r}) \, d\mathbf{r} = 1 \tag{6}$$

defines the TMD amplitude $A(\mathbf{k}_\perp)$. The TMD is then given by

$$P(\mathbf{k}_\perp) = |A(\mathbf{k}_\perp)|^2 \tag{7}$$

and the total ionization flux is

$$P = \int P(\mathbf{k}_\perp) \frac{d\mathbf{k}_\perp}{(2\pi)^2}. \tag{8}$$

Note that in the weak-field limit it coincides with the ionization rate [14]

$$\Gamma|_{F \to 0} = P|_{F \to 0}. \tag{9}$$

The complex energy eigenvalue E and the TMD amplitude $A(\mathbf{k}_\perp)$ are two major observables characterizing the system. They are needed, e.g., for implementing the adiabatic theory [2], where $A(\mathbf{k}_\perp)$ determines the structure of the photoelectron momentum distribution in the transverse with respect to the polarization axis plane.

In studying tunneling ionization of molecules one usually focuses on the dependence of the ionization rate on the orientation of the molecule with respect to the field. We will additionally discuss the TMD. In general, it should be noted that while for a given orientation of the molecule the rate Γ is just a number characterizing the system, the TMD $P(\mathbf{k}_\perp)$ is a function of two variables containing additional information on its structure and ionization dynamics. In particular, the TMD describes vortex electrons generated in tunneling ionization. Indeed, let us introduce polar coordinates in the transverse coordinate $\mathbf{r}_\perp = (x, y) = r_\perp(\cos\varphi, \sin\varphi)$ and momentum $\mathbf{k}_\perp = (k_x, k_y) = k_\perp(\cos\varphi_k, \sin\varphi_k)$ planes. The TMD

amplitude can be expanded in a Fourier series

$$A(\mathbf{k}_\perp) = \sum_{m=-\infty}^{\infty} A_m(k_\perp)e^{im\varphi_k}, \tag{10}$$

where

$$A_m(k_\perp) = \int_0^{2\pi} A(\mathbf{k}_\perp)e^{-im\varphi_k}\frac{d\varphi_k}{2\pi}. \tag{11}$$

Substituting this into Eq. (2) gives

$$\phi(\mathbf{r})|_{z\to-\infty} = \frac{1}{2\pi}\sum_{m=-\infty}^{\infty} e^{im\varphi + i|m|\pi/2}$$
$$\times \int_0^\infty A_m(k_\perp)J_{|m|}(k_\perp r_\perp)g(z, k_\perp)k_\perp dk_\perp. \tag{12}$$

This equation decomposes the outgoing wave into a sum of terms with different projections m of the electron angular momentum on the z axis. The transverse structure of the term with a given m at $r_\perp \to 0$ is determined by a factor $r_\perp^{|m|}e^{im\varphi}$. The term with $m = 0$ represents a locally plane outgoing wave, while terms with $|m| > 0$ describe vortex electrons. Substituting Eq. (10) into (8), the total ionization flux can be presented in the form

$$P = \sum_{m=-\infty}^{\infty} P_m, \tag{13}$$

where

$$P_m = \frac{1}{2\pi}\int_0^\infty |A_m(k_\perp)|^2 k_\perp dk_\perp \tag{14}$$

are partial ionization fluxes characterizing the rate of generation of plane-wave ($m = 0$) or vortex ($|m| > 0$) electrons. Thus, the presence of vortex electrons can be seen from the very fact that the TMD $P(\mathbf{k}_\perp)$ depends on φ_k.

A method to accurately calculate the ionization observables by solving Eq. (1) capable of treating general molecular potentials in a wide range of field strengths was developed in Refs. [3–5]. However, calculations using this method for polyatomic molecules are rather time-consuming and become prohibitively laborious if results for many orientations of the molecule with respect to the field are needed. On the other hand, the WFAT [14] provides an approximate asymptotic solution of the problem in the limit $F \to 0$. The calculations based on the WFAT are feasible for any molecule [16–18], but their results are limited to weak fields.

To explore strong-field effects in tunneling ionization of polyatomic molecules beyond the WFAT, in this paper we employ the ZRP model [21]. The potential for an N-atomic molecule is modeled by a sum of N ZRPs,

$$V(\mathbf{r}) = \sum_{i=1}^N V_{\mathrm{ZRP}}(\mathbf{r} - \mathbf{R}_i; \varkappa_i), \tag{15}$$

where

$$V_{\mathrm{ZRP}}(\mathbf{r}; \varkappa) = \frac{2\pi}{\varkappa}\delta(\mathbf{r})\frac{\partial}{\partial r}r. \tag{16}$$

The vectors $\mathbf{R}_i$ give the positions of the nuclei and are determined by the molecular geometry and its orientation in the laboratory frame, while $\varkappa_i$ are considered as free parameters which can be chosen to reproduce some characteristics of a real molecule affecting its ionization properties. The presence of such an operator potential in Eq. (1) is equivalent to the requirement that the SS eigenfunction must satisfy the boundary conditions [21]

$$\phi(\mathbf{r})|_{\mathbf{r}\to\mathbf{R}_i} = \frac{c_i}{2\pi}\left[\frac{1}{|\mathbf{r} - \mathbf{R}_i|} - \varkappa_i + O(|\mathbf{r} - \mathbf{R}_i|)\right], \tag{17}$$

where

$$c_i = 2\pi|\mathbf{r} - \mathbf{R}_i|\phi(\mathbf{r})|_{\mathbf{r}\to\mathbf{R}_i}. \tag{18}$$

The action of this potential on the eigenfunction is thus given by

$$V(\mathbf{r})\phi(\mathbf{r}) = -\sum_{i=1}^N c_i\delta(\mathbf{r} - \mathbf{R}_i). \tag{19}$$

As shown below, the ionization observables in this model can be calculated without any approximations, even for relatively large N.

III. GREEN'S FUNCTION

The present model is most conveniently analyzed using the outgoing-wave Green's function for an electron in a static electric field $\mathbf{F}$. In this section the field may have an arbitrary direction. The Green's function satisfies

$$\left(-\tfrac{1}{2}\Delta + \mathbf{F}\mathbf{r} - E\right)G(\mathbf{r}, \mathbf{r}'; E) = \delta(\mathbf{r} - \mathbf{r}'). \tag{20}$$

It is usually obtained as the Fourier transform of the corresponding retarded Green's function, which can be found analytically [54], and presented in the form [2]

$$G(\mathbf{r}, \mathbf{r}'; E) = \frac{e^{-i\pi/4}}{(2\pi)^{3/2}}\int_0^\infty \exp\left[iEt + \frac{i(\mathbf{r} - \mathbf{r}')^2}{2t}\right.$$
$$\left. - \frac{i}{2}\mathbf{F}(\mathbf{r} + \mathbf{r}')t - \frac{i}{24}\mathbf{F}^2 t^3\right]\frac{dt}{t^{3/2}}. \tag{21}$$

Recently it has been realized that a similar integral appears in integral representations for products of two solutions of the Airy equation with shifted arguments, which makes it possible to obtain the Green's function in a closed analytic form [55,56]. Using the notation of Ref. [56], the result reads as

$$G(\mathbf{r}, \mathbf{r}'; E) = \frac{-e^{i\pi/6}}{|\mathbf{r} - \mathbf{r}'|}\frac{d}{d\eta}\mathrm{Ai}(\xi + \eta)\mathrm{Ai}\left[e^{2i\pi/3}(\xi - \eta)\right], \tag{22}$$

where

$$\xi = \frac{\mathbf{F}(\mathbf{r} + \mathbf{r}') - 2E}{(2F)^{2/3}}, \quad \eta = \frac{F^{1/3}}{2^{2/3}}|\mathbf{r} - \mathbf{r}'|, \tag{23}$$

and $\mathrm{Ai}(z)$ is the Airy function [57]. It can be seen that in the absence of the field Eq. (22) reduces to the outgoing-wave Green's function for a free electron,

$$G(\mathbf{r}, \mathbf{r}'; E)|_{F\to0} = \frac{e^{ik|\mathbf{r}-\mathbf{r}'|}}{2\pi|\mathbf{r} - \mathbf{r}'|}, \tag{24}$$

where $k = \sqrt{2E}$ and the branch of the square-root function is determined by a branch cut at real positive E, as in scattering theory [58]. The availability of a closed-form expression (22) for the Green's function greatly facilitates this study.

The function (22) diverges as its spatial arguments $\mathbf{r}$ and $\mathbf{r}'$ coalesce. For the following we need its regular part defined by

$$G(\mathbf{r}, \mathbf{r}'; E)|_{\mathbf{r}' \to \mathbf{r}} = \frac{1}{2\pi |\mathbf{r} - \mathbf{r}'|} + G_{\text{reg}}(\mathbf{r}; E). \quad (25)$$

From Eq. (22) we obtain

$$G_{\text{reg}}(\mathbf{r}; E) = -(2F)^{1/3} \big[e^{-i\pi/6} \text{Ai}'(\xi) \text{Ai}'\big(e^{2i\pi/3}\xi\big) \\ + e^{i\pi/6} \xi \text{Ai}(\xi) \text{Ai}\big(e^{2i\pi/3}\xi\big) \big], \quad (26)$$

where primes denote differentiation with respect to the argument of the Airy function. We also need the derivatives of these functions with respect to E given by

$$\frac{\partial G(\mathbf{r}, \mathbf{r}'; E)}{\partial E} = \frac{2^{2/3} e^{i\pi/6}}{F^{1/3}} \text{Ai}(\xi + \eta) \text{Ai}\big[e^{2i\pi/3}(\xi - \eta)\big] \quad (27)$$

and

$$\frac{\partial G_{\text{reg}}(\mathbf{r}; E)}{\partial E} = \frac{2^{2/3} e^{i\pi/6}}{F^{1/3}} \text{Ai}(\xi) \text{Ai}\big(e^{2i\pi/3}\xi\big). \quad (28)$$

The limiting forms of Eqs. (26), (27), and (28) for $F \to 0$ can be easily obtained from Eq. (24).

IV. SIEGERT STATES: EXACT TREATMENT

From here on we restore the convention $\mathbf{F} = F\mathbf{e}_z$. Using the Green's function (22), we rewrite Eq. (1) in the form of a homogeneous integral equation

$$\phi(\mathbf{r}) = -\int G(\mathbf{r}, \mathbf{r}'; E) V(\mathbf{r}') \phi(\mathbf{r}') d\mathbf{r}'. \quad (29)$$

This equation is the basis for the exact calculation of SSs in the ZRP model.

A. Eigenvalue and eigenfunction

We begin with a procedure for calculating the SS eigenvalue and eigenfunction. Our approach generalizes that of Ref. [21], where bound states for $F = 0$ were treated, to SSs in the case $F > 0$. Substituting Eq. (19) into (29) gives

$$\phi(\mathbf{r}) = \sum_{i=1}^{N} c_i G(\mathbf{r}, \mathbf{R}_i; E), \quad (30)$$

where the coefficients c_i are defined by Eq. (18). From this using Eq. (25) we find

$$\phi(\mathbf{r})|_{\mathbf{r} \to \mathbf{R}_i} = \frac{c_i}{2\pi |\mathbf{r} - \mathbf{R}_i|} + c_i G_{\text{reg}}(\mathbf{R}_i; E) \\ + \sum_{j \neq i}^{N} c_j G(\mathbf{R}_i, \mathbf{R}_j; E). \quad (31)$$

Comparing this with Eq. (17), we obtain N coupled equations for the coefficients c_i,

$$\sum_{j=1}^{N} M_{ij}(E) c_j = 0, \quad i = 1, \ldots, N \quad (32)$$

where

$$M_{ij}(E) = \begin{cases} \dfrac{\varkappa_i}{2\pi} + G_{\text{reg}}(\mathbf{R}_i; E), & i = j \\ G(\mathbf{R}_i, \mathbf{R}_j; E), & i \neq j. \end{cases} \quad (33)$$

In order for Eq. (32) to have a nontrivial solution, the determinant of the matrix (33) must turn to zero,

$$\det M_{ij}(E) = 0. \quad (34)$$

This equation defines the SS eigenvalues. The corresponding sets of coefficients c_i solving Eq. (32) define the SS eigenfunctions (30). The normalization condition for the coefficients follows from Eq. (6). Substituting Eq. (30) into (6) gives

$$\sum_{i,j=1}^{N} c_i c_j \int G(\mathbf{r}, \mathbf{R}_i; E) G(\mathbf{r}, \mathbf{R}_j; E) d\mathbf{r} = 1. \quad (35)$$

This can be simplified using Hilbert's identity [59]

$$\int G(\mathbf{r}, \mathbf{r}''; E) G(\mathbf{r}'', \mathbf{r}'; E') d\mathbf{r}'' = \frac{G(\mathbf{r}, \mathbf{r}'; E) - G(\mathbf{r}, \mathbf{r}'; E')}{E - E'}. \quad (36)$$

Setting here $E' \to E$ and taking into account that the Green's function (22) is symmetric with respect to $\mathbf{r}$ and $\mathbf{r}'$, we obtain

$$\sum_{i,j=1}^{N} c_i c_j \frac{\partial M_{ij}(E)}{\partial E} = 1. \quad (37)$$

The derivative of the matrix (33) with respect to E can be calculated using Eqs. (27) and (28). The normalization condition (37) determines the coefficients c_i, and hence the SS eigenfunction (30), up to a common sign.

For any $F > 0$, Eq. (34) has infinitely many generally complex solutions because elements of the matrix (33) are transcendental functions of E. Thus, there are infinitely many SSs. Note that all equations in this subsection remain valid for $F = 0$, with the Green's function given by Eq. (24). In this case Eq. (34) has a finite number $N_b \leqslant N$ of real solutions corresponding to bound states of the field-free system [21]. Let E_n and $\phi_n(\mathbf{r})$, $n = 1, \ldots, N_b$, denote energies and real normalized wave functions of these states. The bound state in Eqs. (4), whose energy and wave function are alternatively denoted by E_0 and $\phi_0(\mathbf{r})$, belongs to this set. As the field is turned on, $F > 0$, bound states turn into tunneling SSs while all the other solutions to Eq. (34) correspond to static-field-induced states [60].

We are interested in one particular SS originating from the bound state of the field-free system modeling the ionizing molecular orbital. Let us summarize the procedure for calculating this SS. We begin with $F = 0$, find all N_b bound states, and select among them the one meant in Eqs. (4). The coefficients solving Eq. (32) for this state are denoted by $c_i^{(0)}$. Then we increment F by small steps, and at each step find the solution to Eqs. (34) and (32) closest to that found at the previous step, which amounts to the analytic continuation of the SS in F. In this way the SS can be continued to arbitrary values of F.

B. Transverse momentum distribution amplitude

We now turn to the calculation of the TMD amplitude. We first discuss the case of an arbitrary potential $V(\mathbf{r})$, which contributes to the development of the general theory of SSs in an electric field [3–5,14,61–63], and then specify the result for the ZRP model. From the definition (2), we have [14]

$$A(\mathbf{k}_\perp) = \left. \frac{1}{g(z, k_\perp)} \int e^{-i\mathbf{k}_\perp \mathbf{r}_\perp} \phi(\mathbf{r}) d\mathbf{r}_\perp \right|_{z \to -\infty}. \quad (38)$$

This formula expresses the TMD amplitude as a surface integral involving the values of the SS eigenfunction only in the asymptotics region $z \to -\infty$. Substituting here Eq. (29) gives

$$A(\mathbf{k}_\perp) = \frac{-1}{g(z, k_\perp)} \int e^{-i\mathbf{k}_\perp \mathbf{r}_\perp} G(\mathbf{r}, \mathbf{r}'; E) V(\mathbf{r}')$$
$$\times \left. \phi(\mathbf{r}') d\mathbf{r}' d\mathbf{r}_\perp \right|_{z \to -\infty}. \quad (39)$$

The asymptotics of the Green's function (22) at $z \to -\infty$ depends on the value of $|\mathbf{r}_\perp - \mathbf{r}'_\perp|$. As will become clear shortly, for substituting into Eq. (39) we need the asymptotics in the region $|\mathbf{r}_\perp - \mathbf{r}'_\perp| = O(|z|^{1/2})$. In this region [see Eqs. (23)]

$$\xi = -\frac{F^{1/3}|z|}{2^{2/3}} + \frac{Fz' - 2E}{(2F)^{2/3}}, \quad (40a)$$

$$\eta = \frac{F^{1/3}}{2^{2/3}} \left[|z| + z' + \frac{(\mathbf{r}_\perp - \mathbf{r}'_\perp)^2}{2|z|} + O(|z|^{-1}) \right]. \quad (40b)$$

The asymptotics we need is given by

$$G(\mathbf{r}, \mathbf{r}'; E)|_{z \to -\infty} = \frac{e^{-i\pi/4}(2F)^{1/12}}{2\pi^{1/2}|z|^{3/4}} \mathrm{Ai}(\xi + \eta)$$
$$\times \exp\left[\frac{iF^{1/2}|2z|^{3/2}}{3} + \frac{iE|2z|^{1/2}}{F^{1/2}} \right.$$
$$\left. + \frac{iF^{1/2}(\mathbf{r}_\perp - \mathbf{r}'_\perp)^2}{2^{3/2}|z|^{1/2}} \right]. \quad (41)$$

The last term in the exponent here scales as $O(|z|^{1/2})$. Therefore, the exponential is a rapidly oscillating function of $\mathbf{r}_\perp$ at $z \to -\infty$, and in this limit the integral over $\mathbf{r}_\perp$ in Eq. (39) can be calculated using the saddle-point method. The only saddle point is given by

$$\mathbf{r}_\perp = \mathbf{r}'_\perp + \frac{|2z|^{1/2}}{F^{1/2}} \mathbf{k}_\perp. \quad (42)$$

This equation has a simple physical meaning. Let an electron interacting with the field $\mathbf{F} = F\mathbf{e}_z$ begin its motion at $\mathbf{r}' = (\mathbf{r}'_\perp, z')$ with the initial velocity $\mathbf{k} = (\mathbf{k}_\perp, k_z)$. Then its coordinate $\mathbf{r} = (\mathbf{r}_\perp, z)$ as a function of time t is given by $\mathbf{r}_\perp = \mathbf{r}'_\perp + \mathbf{k}_\perp t$ and $z = z' + k_z t - Ft^2/2$. The limit $z \to -\infty$ corresponds to $t \to \infty$. In this limit $t = (2|z|/F)^{1/2}$, which leads to Eq. (42). The asymptotics (41) must hold in the region of $\mathbf{r}_\perp$ including the saddle point (42), which explains the values of $|\mathbf{r}_\perp - \mathbf{r}'_\perp|$ considered. Calculating the integral, we obtain

$$A(\mathbf{k}_\perp) = -\frac{e^{i\pi/4}2\pi^{1/2}}{(2F)^{1/6}} \int e^{-i\mathbf{k}_\perp \mathbf{r}_\perp} \mathrm{Ai}\left(\frac{2Fz + k_\perp^2 - 2E}{(2F)^{2/3}} \right)$$
$$\times V(\mathbf{r})\phi(\mathbf{r}) d\mathbf{r}. \quad (43)$$

This formula is a new result in the theory of SSs. It expresses the TMD amplitude in the form of a volume integral or a matrix element involving the SS eigenfunction values in the region of localization of the potential $V(\mathbf{r})$. We emphasize that Eqs. (38) and (43) are equally exact, but for their implementation one needs to know the SS eigenfunction in different regions of space. Similar exact integral representations for partial amplitudes of ionization into the different parabolic channels were obtained in Ref. [62]. It is well known that integral representations for observables appearing as coefficients in the asymptotic tail of the corresponding wave function, such as the elastic scattering amplitude [58], play an important role in the theory.

The usefulness of Eq. (43), in particular, is illustrated by the fact that the TMD amplitude in the ZRP model immediately follows from this formula upon substituting Eq. (19):

$$A(\mathbf{k}_\perp) = \frac{e^{i\pi/4}2\pi^{1/2}}{(2F)^{1/6}} \sum_{i=1}^{N} c_i e^{-i\mathbf{k}_\perp \mathbf{R}_{i\perp}} \mathrm{Ai}\left(\frac{2FR_{iz} + k_\perp^2 - 2E}{(2F)^{2/3}} \right). \quad (44)$$

This is an exact result which holds for any field strength. The dependence of this TMD amplitude on F, including that hidden in the eigenvalue E and the coefficients c_i, is nontrivial. But for a given F, hence given E and c_i, its dependence on $\mathbf{k}_\perp$ is explicit and can be explored analytically. From Eq. (44) we obtain partial TMD amplitudes (11) in the ZRP model

$$A_m(k_\perp) = \frac{e^{i\pi/4 - i|m|\pi/2}2\pi^{1/2}}{(2F)^{1/6}} \sum_{i=1}^{N} c_i e^{-im\Phi_i} J_{|m|}(k_\perp R_{i\perp})$$
$$\times \mathrm{Ai}\left(\frac{2FR_{iz} + k_\perp^2 - 2E}{(2F)^{2/3}} \right), \quad (45)$$

where we introduced the notation $\mathbf{R}_{i\perp} = (R_{ix}, R_{iy}) = R_{i\perp}(\cos\Phi_i, \sin\Phi_i)$. The partial ionization fluxes (14) can be obtained using Eq. (45) by integrating over $k_\perp$ numerically. Note that if the SS eigenfunction has a plane of mirror symmetry passing through the z axis, then the TMD amplitude (38) has a line of mirror symmetry passing through the origin in the $\mathbf{k}_\perp$ plane. In this case $A_{|m|}(\mathbf{k}_\perp)$ and $A_{-|m|}(\mathbf{k}_\perp)$ differ only by a phase factor, and therefore $P_{|m|} = P_{-|m|}$.

C. Rotation of the molecule

Here we discuss the dependence of the SS on the orientation of the molecule with respect to the field. In the ZRP model, this dependence enters the theory only through the nuclear coordinates $\mathbf{R}_i$ in the laboratory frame (LF). Let $\mathbf{R}'_i$ denote the nuclear coordinates in a molecular frame (MF); these vectors are determined by the geometry of the molecule and assumed to be given. The orientation of the molecule is specified by the three Euler angles (α, β, γ) defining a rotation from the LF to the MF [64]. The SS eigenvalue E does not depend on α. The TMD amplitude does depend on α, but this dependence is rather simple. Considering $A(\mathbf{k}_\perp)$ at a given orientation as a function of polar coordinates $(k_\perp, \varphi_k)$, it can be seen that

$$A(k_\perp, \varphi_k)|_{\alpha,\beta,\gamma} = A(k_\perp, \varphi_k - \alpha)|_{\alpha=0,\beta,\gamma}. \quad (46)$$

Thus, without loss of generality, we can set $\alpha = 0$. In this case

$$R_{ix} = R'_{ix} \cos\beta \, \cos\gamma - R'_{iy} \cos\beta \, \sin\gamma + R'_{iz} \sin\beta, \quad (47a)$$

$$R_{iy} = R'_{ix} \sin\gamma + R'_{iy} \cos\gamma, \quad (47b)$$

$$R_{iz} = -R'_{ix} \sin\beta \, \cos\gamma + R'_{iy} \sin\beta \, \sin\gamma + R'_{iz} \cos\beta. \quad (47c)$$

Substituting this into the above equations makes the SS dependent on the orientation angles β and γ.

V. WEAK-FIELD ASYMPTOTICS

In the WFAT [14], the solution to Eqs. (1), (2), and (4) is obtained in the form of an asymptotic expansion in F for $F \to 0$. This asymptotics provides a reference helpful for comparison with exact calculations. Here we summarize the leading-order WFAT results for the ZRP model. We begin with the field-shifted energy $\mathcal{E}$ of the state. Tunneling ionization is exponentially suppressed at $F \to 0$ and can be neglected in obtaining $\mathcal{E}$. This leads to the perturbation-theory expansion

$$\mathcal{E} = E_0 - \mu_z F + O(F^2), \quad (48)$$

where μ_z is the z component of the dipole moment in the unperturbed bound state in the LF,

$$\boldsymbol{\mu} = -\int \mathbf{r}\phi_0^2(\mathbf{r})d\mathbf{r}. \quad (49)$$

Using Eq. (30) and taking into account that the field-free Green's function (24) depends only on the distance $|\mathbf{r} - \mathbf{r}'|$ between its spatial arguments, in the ZRP model we obtain

$$\boldsymbol{\mu} = -\frac{1}{2}\sum_{i,j=1}^{N}(\mathbf{R}_i + \mathbf{R}_j)c_i^{(0)}c_j^{(0)}\frac{\partial M_{ij}(E)}{\partial E}\bigg|_{F=0,E=E_0}. \quad (50)$$

In practice, it is more convenient to calculate the dipole moment $\boldsymbol{\mu}'$ in the MF once and then use

$$\mu_z = (-\mu'_x \cos\gamma + \mu'_y \sin\gamma)\sin\beta + \mu'_z \cos\beta \quad (51)$$

to find μ_z for different orientations of the molecule. Neglecting ionization in the ZRP model amounts to projecting Eq. (1) onto the subspace of N_b unperturbed bound states. This leads to an algebraic eigenvalue problem

$$\det[(E_n - \mathcal{E})\delta_{nm} + Fz_{nm}] = 0, \quad (52)$$

where

$$z_{nm} = \int \phi_n(\mathbf{r})z\phi_m(\mathbf{r})d\mathbf{r}. \quad (53)$$

In the limit $F \to 0$ this equation reproduces the expansion (48). Note, however, that as F grows the expansion holds up to the first encounter of a point of nonanalyticity of the SS eigenvalue E as a function of F. In the ZRP model such nonanalyticities correspond to branch points connecting different sheets of the Riemann surface of E considered as a multivalued analytic function of complex F. Meanwhile, Eq. (52) holds as long as ionization can be neglected, which may remain valid far beyond the range of applicability of Eq. (48). The eigenvalues of Eq. (52) are real and we denote them by $\mathcal{E}_n$, $n = 1, \ldots, N_b$. We will see that they provide a

very good approximation for real parts of the SS eigenvalues originating from bound states of the system.

The ionization observables are obtained in the WFAT by expanding the outgoing flux in parabolic channels $\nu = (n_\xi, m)$, where $n_\xi = 0, 1, \ldots$ and $m = 0, \pm 1, \ldots$ are parabolic quantum numbers [14]. Channels with $m = 0$ and $|m| > 0$ correspond to plane-wave and vortex electrons, respectively. The leading-order contribution to a partial ionization flux P_m comes from the channel $\nu = (0, m)$,

$$P_m|_{F \to 0} = |G_{0m}|^2 W_{0m}, \quad (54)$$

where

$$G_{0m} = e^{-\varkappa\mu_z}g_{0m} \quad (55)$$

is the structure factor and

$$W_{0m} = \frac{\varkappa}{2}\left(\frac{F}{4\varkappa^2}\right)^{1+|m|}\exp\left[-\frac{2\varkappa^3}{3F}\right] \quad (56)$$

is the field factor [14,65]. Here $\varkappa = \sqrt{2|E_0|}$ and g_{0m} is an asymptotic coefficient characterizing the ionizing orbital. Using the integral representation for g_ν obtained in Ref. [62], we find that in the ZRP model

$$g_{0m} = \frac{2\varkappa^{(|m|-1)/2}}{\sqrt{2\pi|m|!}}\sum_{i=1}^{N}c_i^{(0)}R_{i\perp}^{|m|}e^{-im\Phi_i}e^{-\varkappa R_{iz}}. \quad (57)$$

Channels with $n_\xi > 0$ contribute to P_m terms with increasingly higher powers of the small parameter F. It can be seen from Eqs. (9), (13), and (56) that the leading-order contribution to the ionization rate comes from the channel $\nu = (0, 0)$ and coincides with P_0,

$$\Gamma|_{F \to 0} = |G_{00}|^2 W_{00}. \quad (58)$$

This asymptotics holds provided that $G_{00} \neq 0$. The asymptotic coefficient g_{00} can be alternatively represented by

$$g_{00} = \sqrt{\frac{2\pi}{\varkappa}}|2z|e^{-\varkappa z}\phi_0(\mathbf{r})\bigg|_{x=y=0, \, z \to -\infty}. \quad (59)$$

This shows that the structure factor for the dominant ionization channel G_{00} reflects the shape of the ionizing orbital $\phi_0(\mathbf{r})$. In particular, it turns to zero at orientations where the negative z semiaxis either belongs to or asymptotically approaches a nodal surface of $\phi_0(\mathbf{r})$. At such orientations the leading-order contribution to Γ comes from channels $\nu = (0, \pm 1)$.

We now turn to the TMD amplitude. In the present model we have the exact expression (44), so the weak-field asymptotics can be derived directly from it. Substituting there E from Eq. (48) and $c_i^{(0)}$ for c_i gives

$$A(\mathbf{k}_\perp)|_{F \to 0} = \frac{e^{i\pi/4}}{(\varkappa^2 + k_\perp^2)^{1/4}}\exp\left[-\frac{(\varkappa^2 + k_\perp^2)^{3/2}}{3F}\right]$$

$$\times \sum_{i=1}^{N}c_i^{(0)}e^{-i\mathbf{k}_\perp \mathbf{R}_{i\perp}}e^{-\sqrt{\varkappa^2 + k_\perp^2}(\mu_z + R_{iz})}. \quad (60)$$

This asymptotics holds for $F \to 0$ uniformly in $k_\perp$. In the region $k_\perp \ll (\varkappa F)^{1/4}$ we obtain

$$A(\mathbf{k}_\perp)|_{F\to 0} = e^{i\pi/4}\sqrt{\frac{\pi}{2}} \exp\left[-\frac{\varkappa^3}{3F} - \frac{\varkappa k_\perp^2}{2F}\right]$$
$$\times \left[G_{00} - \frac{ik_\perp}{\sqrt{\varkappa}}|G_{01}|\cos(\varphi_k + \gamma_{01})\right], \quad (61)$$

where $\gamma_{01} = \arg G_{01}$ and we have taken into account that $G_{0,-m} = G_{0m}^*$. We retained in Eq. (61) only the leading-order terms for channels $\nu = (0,0)$ and $(0,\pm 1)$. This asymptotics agrees with the WFAT result [14]. If $G_{00} \neq 0$, the TMD (7) as a function of $\mathbf{k}_\perp$ has a Gaussian shape,

$$P(\mathbf{k}_\perp)|_{F\to 0} \propto \exp\left[-\frac{\varkappa k_\perp^2}{F}\right]. \quad (62)$$

This is the basic shape of the TMD in the limit $F \to 0$ for any one-electron system. The only information about the ionizing orbital contained in Eq. (62) is represented by the parameter $\varkappa$. At orientations where $G_{00} = 0$ but $G_{0\pm 1} \neq 0$, the shape of the TMD is described by

$$P(\mathbf{k}_\perp) \propto k_\perp^2 \cos^2(\varphi_k + \gamma_{01}) \exp\left[-\frac{\varkappa k_\perp^2}{F}\right]. \quad (63)$$

Here an additional characteristic γ_{01} of the orbital appears. In general, one can expect that contributions to the TMD from vortex electrons with larger $|m|$ contain more structural information. We will see shortly that this is indeed the case.

VI. ILLUSTRATIVE RESULTS AND DISCUSSION

The main advantage of the ZRP model stems from the fact that it allows one to accurately calculate tunneling ionization observables for polyatomic molecules with complex geometry. However, before discussing the results, let us indicate some drawbacks of the model which should be kept in mind in the following. The most important drawback is that each individual ZRP supports only one bound state of s symmetry. As a result, molecular orbitals have a grapelike shape (see Figs. 1, 6, 12 below). Orbitals with, e.g., p-like behavior at atomic nuclei are not reproduced by the model, which limits the variety of shapes of the ionizing orbital that can be treated. Another specific feature of the ZRP model is that there is not a distinct transition from tunneling to over-the-barrier ionization regime as the field strength grows. Finally, this model inherits the major drawback of the SAEA, namely, the one-electron binding potential is assumed to be unaffected by the ionizing field.

In the illustrative calculations we consider three molecules whose geometries reproduce that of the real water, benzene, and leucine molecules. The parameters $\varkappa_i$ are chosen as explained below. In all the cases the number of bound states coincides with the number of atoms, $N_b = N$. We consider ionization from the highest bound state. The shape of this orbital differs from that of the highest occupied molecular orbital (HOMO) in the real water molecule, etc. To emphasize the difference, we will call our model molecules a water *like* molecule, etc.
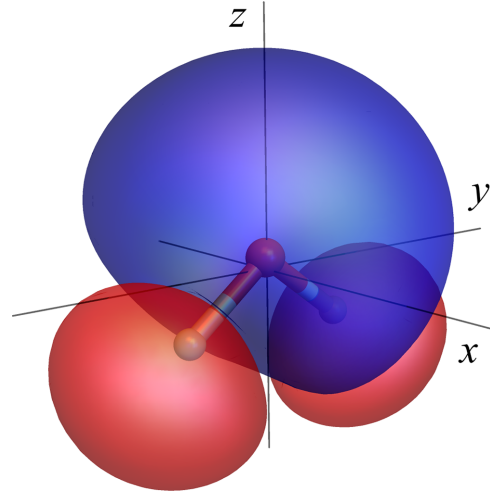

FIG. 1. The unperturbed ionizing orbital of the waterlike molecule at the orientation $(\beta, \gamma) = (0°, 0°)$. An isosurface of $|\phi_0(\mathbf{r})|$ is shown, with the different colors encoding the sign of $\phi_0(\mathbf{r})$.

A. Simplest nonlinear waterlike molecule

To begin with, we discuss a waterlike molecule, that is, a model of H_2O described by $N = 3$ ZRPs. This is a nonlinear molecule, the first nontrivial in terms of geometry example on the way from atoms [23] through diatomics [24,25] to polyatomic molecules, and it is instructive to analyze how its structure is reflected in the ionization observables. At the same time, this is still a rather simple molecule which admits a detailed analysis. We mention that calculations of the ionization rate from the HOMO of the real water molecule within the WFAT were reported in Ref. [66]. Ionization rates for this molecule obtained in the SAEA with a more realistic potential [8] and in *ab initio* coupled-cluster calculations [11] were also reported.

To define the model, we need to specify the nuclear coordinates $\mathbf{R}_i'$ in the MF and the parameters $\varkappa_i$. We use the same coordinates as in Ref. [66], namely, $\mathbf{R}_{H_{1,2}}' = (0, \pm 1.431, -0.887)$, where the subscripts H_1 and H_2 refer to the two hydrogen nuclei, and $\mathbf{R}_O' = (0, 0, 0.222)$. The energy of the HOMO in H_2O and its dipole moment in the MF calculated using the density functional theory are $E_0 = -0.464$ and $\boldsymbol{\mu}' = (0, 0, -0.135)$ [66]. The parameters $\varkappa_H = 1.276$ and $\varkappa_O = 1.019$ are chosen so that the highest bound state in the ZRP model reproduces these characteristics of the real water molecule. With these parameters, the energies of the other two lower-lying bound states are $E_1 = -0.850$ and $E_2 = -0.803$ and their dipole moments are $\boldsymbol{\mu}_1' = (0, 0, 0.789)$ and $\boldsymbol{\mu}_2' = (0, 0, 0.887)$.

The ionizing orbital of the waterlike molecule is shown in Fig. 1. This figure corresponds to the orientation $(\beta, \gamma) = (0°, 0°)$ at which the LF and MF coincide. It illustrates a drawback of the ZRP model mentioned above. The molecule has a mirror symmetry plane passing through the nuclei, thus, all molecular orbitals are either even or odd functions under reflection with respect to this plane. The HOMO of the real molecule is an odd function, which means that it has zero amplitudes at all nuclei. However, such an orbital would not feel the presence of the ZRPs and therefore cannot be reproduced
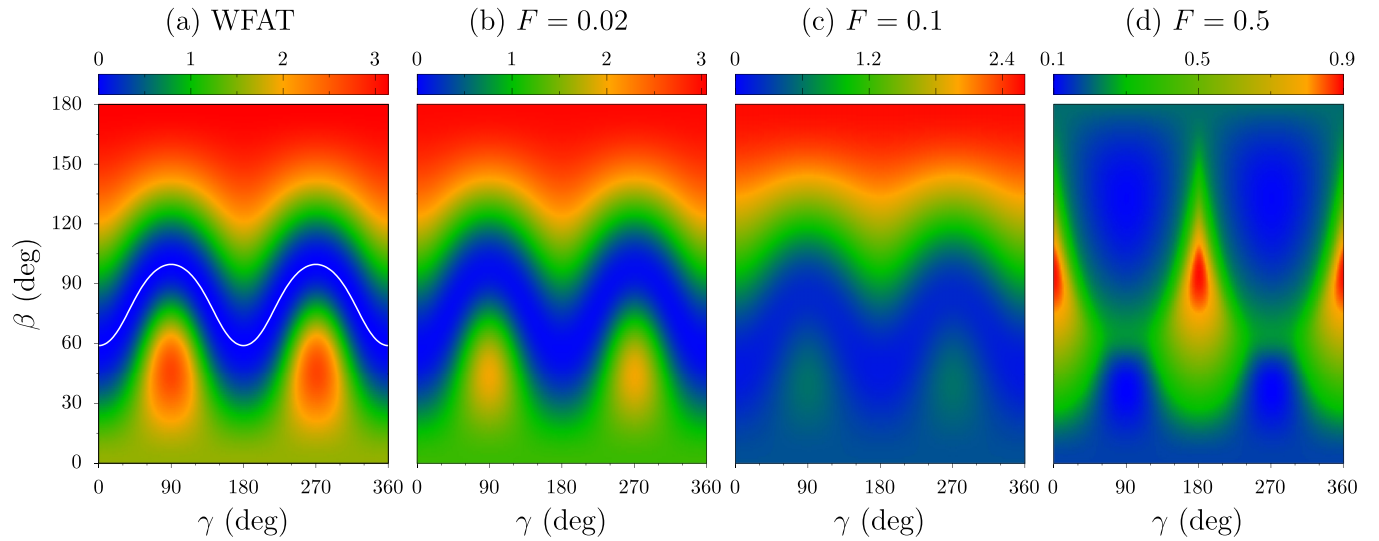
FIG. 2. The ratio Γ/W_{00} of the ionization rate to the field factor for the waterlike molecule as a function of the orientation angles (β, γ). (a) The WFAT results given by the structure factor squared $|G_{00}|^2$ [see Eq. (58)]. The white line shows the zero of G_{00} reflecting the nodal surface of the unperturbed ionizing orbital $\phi_0(\mathbf{r})$. (b)–(d) Exact results for field strengths $F = 0.02$, 0.1, and 0.5. The corresponding values of the field factor are $W_{00} = 2.9 \times 10^{-16}$, 3.3×10^{-5}, and 2.0×10^{-2}, respectively.

by the ZRP model. The shape of the orbital shown in Fig. 1 is qualitatively similar to that of HOMO-1 in the real water molecule.

Figure 2 shows the ionization rate as a function of the orientation angles (β, γ). To eliminate the very strong dependence on the field strength, the rate is divided by the field factor W_{00} for the dominant ionization channel [see Eq. (56)]. In the weak-field limit the ratio does not depend on F and is given by $|G_{00}|^2$ [see Eq. (58)]. These leading-order WFAT results are shown in Fig. 2(a). The white line shows the zero of G_{00} which reflects the nodal surface of the ionizing orbital passing between the O and H nuclei (see Fig. 1). The main maximum of $|G_{00}|^2$ at $\beta = 180°$ corresponds to the major lobe of the orbital centered at the O nucleus. The two lower maxima at $(45°, 90°)$ and $(45°, 270°)$ correspond to the lobes located at the H nuclei. All this confirms the general belief that the orientation dependence of the ionization rate reflects the shape of the ionizing orbital [67–72]. Equation (59) justifies this belief in the weak-field limit.

The other panels in Fig. 2 show exact results calculated for three representative field strengths. Figure 2(b) shows results for a relatively weak field $F = 0.02$ (corresponding to intensity 1.4×10^{13} W/cm^2). In this case the exact results quantitatively agree with the prediction of the WFAT. They reproduce the valley surrounding the nodal line of $|G_{00}|^2$ and all three of its maxima. It should be noted, however, that the exact ionization rate does not turn to zero where $|G_{00}|^2$ does because there are contributions from the $\nu = (0, \pm 1)$ and higher channels not included in Eq. (58). Furthermore, one can notice that the two lower maxima become slightly less pronounced compared to the WFAT results. This can be explained by a distortion of the ionizing orbital caused by the field. Such a distortion was found in time-dependent calculations [73–78] and within the strong-field approximation [79]. It is accounted for by the first-order correction terms

in the WFAT [61], as was demonstrated by the analysis of tunneling ionization of H$_2^+$ in Ref. [80]. Figure 2(c) shows results for a typical field $F = 0.1$ used in strong-field physics (corresponding to intensity 3.5×10^{14} W/cm^2). One can see that although there remains similarity with the WFAT results, both in the absolute values of the ionization rate and its dependence on the orientation angles, the overall picture is much more distorted. The situation changes dramatically as the field grows further. Figure 2(d) shows results for a rather strong but realistic field $F = 0.5$ (corresponding to intensity 8.8×10^{15} W/cm^2). The shape of the orientation dependence of the ionization rate in this case qualitatively differs from that at weaker fields. If the variation of the shape in Figs. 2(a)–2(c) can be attributed to the distortion of the ionizing orbital caused by the field, then a qualitative restructuring of the orbital should occur somewhere in the interval between $F = 0.1$ and 0.5.

To explain this effect, let us consider real parts of the energy eigenvalues for three SSs originating from the three bound states of the system as functions of F shown by solid lines in Fig. 3. At sufficiently weak fields all the energies behave linearly in F, in agreement with Eq. (48). Their behavior in this region is determined by the z component of the dipole moment of the corresponding unperturbed orbital in the LF. At the orientation $(0°, 0°)$ shown in the top panel the MF and LF coincide. The dipole moment of the highest state, ionization from which we consider, is negative, therefore, its energy goes up, while the dipole moments of the two lower states are positive, so their energies go down. At this orientation the states do not cross. However, the signs of the dipoles change to the opposite as the molecule is rotated to the orientation $(180°, 0°)$ shown in the bottom panel. Now the energy of the highest state goes down and the energies of the lower states go up. This results in an avoided crossing between the highest and the lowest states near $F = 0.25$; the middle state is not coupled to them by the field at this orientation.
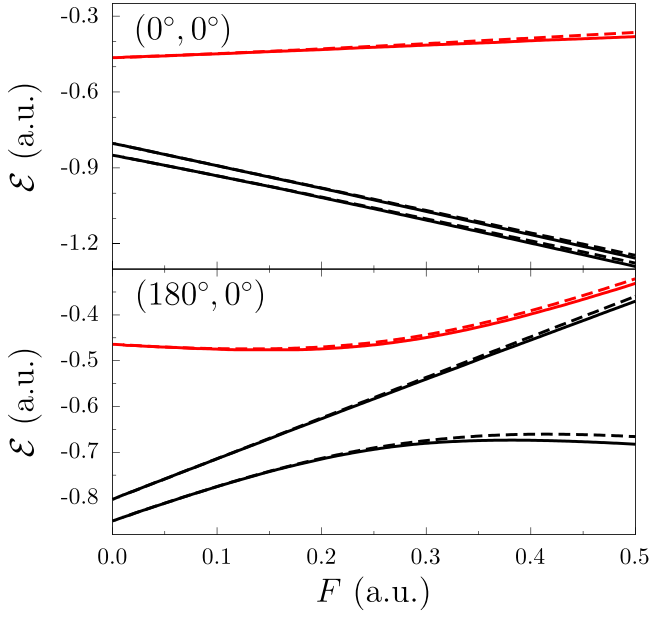
FIG. 3. Real parts of the energy eigenvalues (5) for three SSs originating from the three bound states of the waterlike molecule as functions of the field strength F at two orientations (β, γ). Solid lines show the exact results obtained by solving Eq. (34), dashed lines show approximate results obtained from Eq. (52). Top (red) lines correspond to the ionizing orbital.

This avoided crossing is a manifestation of a branch point connecting the states in the complex F plane. When the states pass through the avoided crossing as F grows, they interchange their identities, so the shape of the ionizing orbital changes qualitatively, and this is reflected in Fig. 2(d). The dashed lines in Fig. 3 show real energies $\mathcal{E}_n$ obtained by neglecting ionization from Eq. (52). They are in very good agreement with the real parts of the exact SS eigenvalues. The matrix in Eq. (52) is Hermitian, and avoided crossings of eigenvalues of such a matrix as functions of some parameter is a well-known phenomena in the theory of nonadiabatic transitions [81]. Note that the matrix z_{nm} in Eq. (52) depends on the orientation of the molecule, and hence so do the positions of avoided crossings in F.

Figure 4 shows TMDs calculated for two stronger fields of those considered in Fig. 2 at four representative orientations of the molecule illustrated in the top row. To bring all panels for the same value of F to a common scale, the TMDs are divided by the ionization rate. Figure 5 helps to understand the results shown in Fig. 4. Solid lines in this figure show partial ionization fluxes, also divided by the ionization rate, calculated for the same orientations as in Fig. 4 as functions of F. For the present molecule at all the orientations considered we have $P_{|m|} = P_{-|m|}$, for the reason explained below Eq. (45), so the lines with $|m| > 0$ in Fig. 5 show the sum $(P_{|m|} + P_{-|m|})/\Gamma$. The sum of all P_m gives the total ionization flux [see Eqs. (8) and (13)], which in the weak-field limit coincides with the
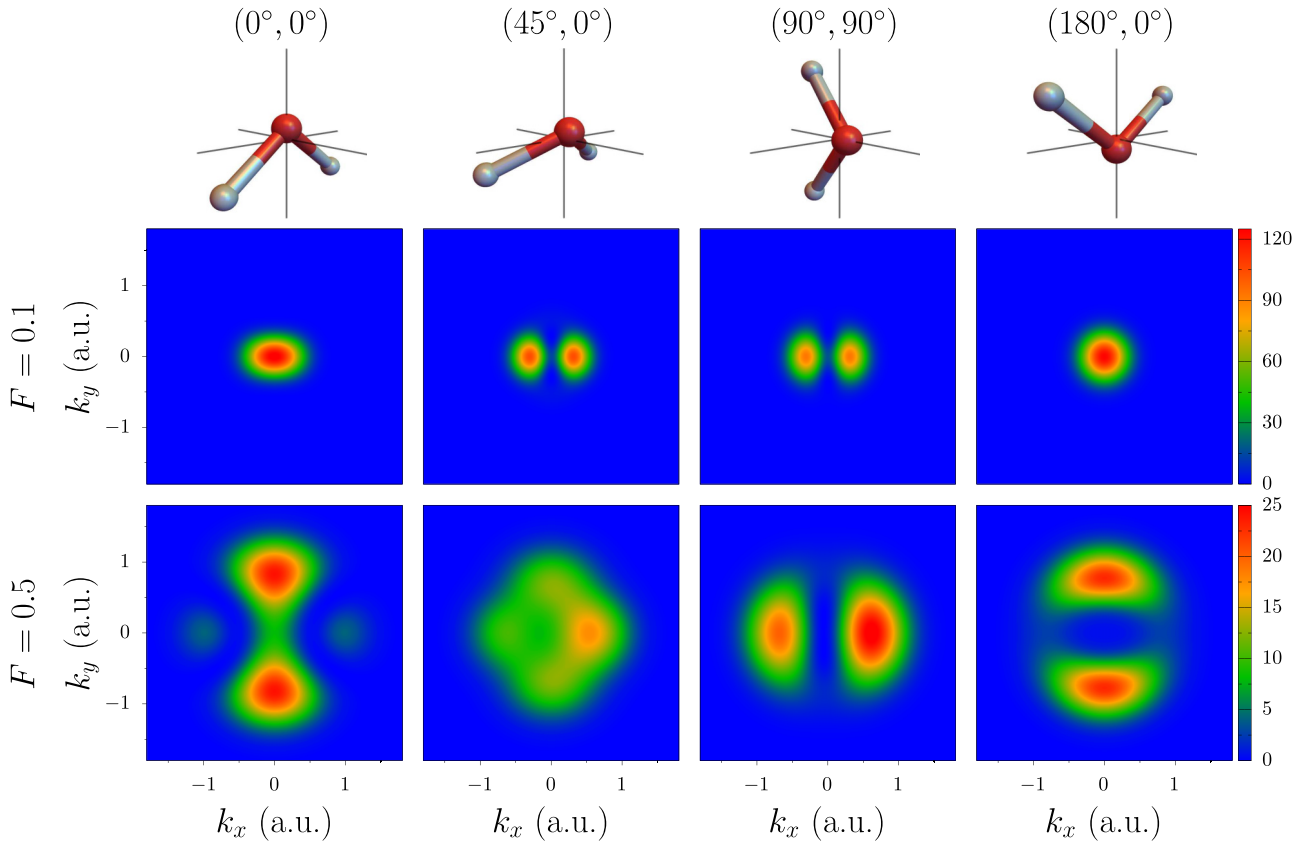

FIG. 4. The ratio $P(\mathbf{k}_\perp)/\Gamma$ of the TMD to the ionization rate for the waterlike molecule as a function of the transverse momentum $\mathbf{k}_\perp = (k_x, k_y)$ at four representative orientations (β, γ) of the molecule indicated and illustrated in the top row. The middle and bottom rows show the exact results for field strengths $F = 0.1$ and 0.5, respectively.
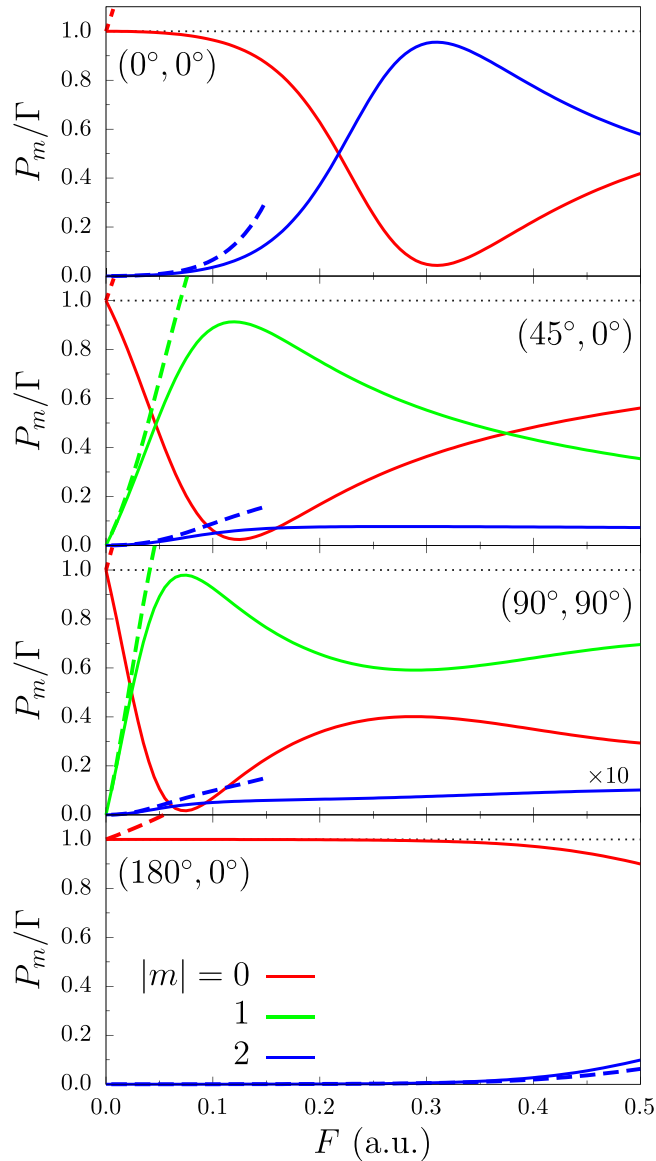
FIG. 5. Ratios P_m/Γ of partial ionization fluxes to the ionization rate for the waterlike molecule as functions of the field strength F for the same four orientations (β, γ) as in Fig. 4. Solid lines show the exact results calculated using Eqs. (14) and (45), dashed lines show the WFAT results obtained from Eq. (54). In all the cases $P_{-|m|} = P_{|m|}$, so the lines with $|m| > 0$ show the sum $(P_{|m|} + P_{-|m|})/\Gamma$. In the top and bottom panels $P_1 = P_{-1} = 0$.

ionization rate [see Eq. (9)]. Our calculations confirm that this equality holds very well: the difference between Γ and P grows with F, but remains within 0.16% for the strongest field $F = 0.5$ considered. Partial fluxes for only three smallest values of $|m|$ are shown in Fig. 5; the higher vortex fluxes are not visible on the scale of the figure. Note that for orientations corresponding to the top and bottom panels $P_1 = P_{-1} = 0$ because the SS eigenfunction in this case is even with respect to two reflections $x \to -x$ and $y \to -y$ simultaneously.

We first discuss the TMDs shown in Fig. 4 for the weaker field $F = 0.1$. As can be expected from Fig. 2, their shapes can be understood, at least qualitatively, using the WFAT.

Indeed, consider the left and right panels. These orientations are far from the nodal line of G_{00} [see Fig. 2(a)]. Therefore, the ionization flux is dominated by the plane-wave electrons with $m = 0$, as can be seen from the top and bottom panels in Fig. 5. As a result, the TMDs have more or less Gaussian shapes, in agreement with Eq. (62). Consider now the two middle panels. These orientations are close to the nodal line of G_{00}. In this case the ionization flux is dominated by vortex electrons with $|m| = 1$, as is confirmed by the two middle panels in Fig. 5. Taking into account that for these orientations $\gamma_{01} = 0$, the shapes of the TMDs agree with Eq. (63). The radius of the TMDs in the $\mathbf{k}_\perp$ plane estimated from the exponential factor in Eqs. (62) and (63) is $k_\perp \sim \sqrt{F/\varkappa} \approx 0.3$, which agrees with the calculations. Note that in all the cases the TMDs are dominated by a single $|m|$. This is a generic feature of TMDs in the weak-field limit explained by the fact that channels with different $|m|$ have different powers of the small parameter F in the field factor (56). Dashed lines in Fig. 5 show partial ionization fluxes calculated using the leading-order WFAT [Eq. (54)]. This asymptotics correctly reproduces the behavior of P_m at $F \to 0$. The relative difference between the WFAT and exact results grows as $O(F)$ and is accounted for by the first-order WFAT [61].

We now turn to the TMDs for the stronger field $F = 0.5$. Their radii in $k_\perp$ are slightly larger than $\sqrt{F/\varkappa} \approx 0.7$ predicted by the WFAT. More importantly, they demonstrate a greater variety of shapes. This is explained by the growing role of the contribution from vortex electrons with $|m| > 0$ to the total ionization flux at stronger fields (see Fig. 5). The left and right panels in Fig. 4 show the result of the interference of contributions from the $m = 0$ and $|m| = 2$ channels, as can be seen from the top and bottom panels in Fig. 5. The shapes shown in the two middle panels in Fig. 4 result from the interference of channels with $m = 0$ and $|m| = 1$, as can be seen from the two middle panels in Fig. 5. Thus, the interference of several channels with different $|m|$ and comparable amplitudes becomes a generic feature of TMDs at stronger fields.

Let us show that the interference pattern in such TMDs encodes information on the structure of the molecule. Consider, for example, the TMD for the field strength $F = 0.5$ at the orientation $(0°, 0°)$ (see Fig. 4). It is described by an analytically known function (44). For the present orientation $c_{H_1} = c_{H_2} = c_H$ and $\mathbf{R}_{H_{1,2}} = (0, \pm R_{Hy}, R_{Hz})$. Thus, the TMD obtained from Eq. (44) contains four complex c_H, c_O, $E - R_{Hz}$, and $E - R_{Oz}$ and one real R_{Hy} parameters. Note that the difference between $E - R_{Hz}$ and $E - R_{Oz}$ equal to $R_{Oz} - R_{Hz}$ and R_{Hy} determine the molecular geometry. It is possible to find these parameters by fitting a given TMD by Eq. (44). Since the exact TMD was obtained from Eq. (44), the fit should return the exact values of the parameters. To mimic some uncertainty in the fitting data, we fit the exact TMD by Eq. (44) assuming that all the parameters are real. The geometrical parameters obtained in this way are $(R_{Oz} - R_{Hz})_{\text{fit}} = 1.20$ and $(R_{Hy})_{\text{fit}} = 0.738$, while their exact values are $R_{Oz} - R_{Hz} = 1.11$ and $R_{Hy} = 0.715$. This example demonstrates that the TMD encodes structural information and, in principle, the geometry of a molecule can be extracted from the TMD measured at a single orientation. We mention that a similar procedure applied for $F = 0.1$ at the same orientation is less stable because the TMD in
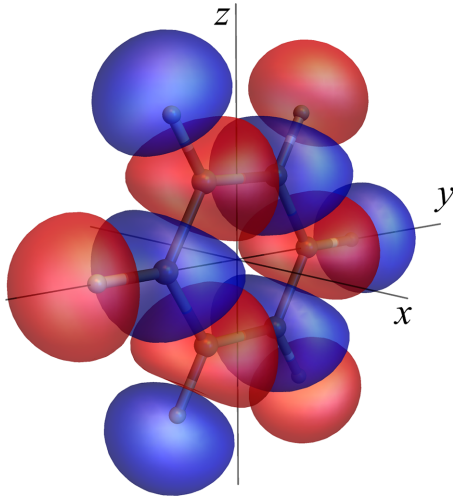
FIG. 6. The unperturbed ionizing orbital, similar to Fig. 1, but for the benzenelike molecule.

this case has less structure and the fit is less sensitive to the parameters.

Summarizing this subsection, we conclude the following. First, because of avoided crossings, the ionizing orbital may undergo a qualitative restructuring as the field grows, and this is reflected in the orientation dependence of the ionization rate. Second, the relative contribution of vortex electrons with $|m| > 0$ to the total ionization flux grows with F, that is, vortex electrons are generated in tunneling ionization more efficiently. Third, this leads to the appearance of a rich interference structure in the TMD which contains information on the geometry of the molecule.

B. Aromatic benzenelike molecule

We next discuss a more complex benzenelike molecule, a model of C_6H_6 described by $N = 12$ ZRPs. This is a highly symmetric molecule and it is interesting to see how its symmetries are reflected in the ionization observables. The internuclear distances are taken from the NIST Chemistry WebBook [82]. We place all nuclei in the (y, z) plane symmetrically with respect to the origin, as shown in Fig. 6. The energy of the HOMO in the real benzene is $E_0 = -0.340$ [82,83] and its dipole moment is zero. In this case, we define the parameters $\varkappa_i$ by

$$\varkappa_i = c\sqrt{2I_i}, \tag{64}$$

where I_i is the ionization potential of the corresponding isolated atom. The common for all nuclei coefficient $c = 1.023$ is chosen such that the energy of the highest bound state coincides with E_0; its dipole moment is automatically zero because of the symmetry. This gives $\varkappa_C = 0.931$ and $\varkappa_H = 1.023$. Figure 6 shows the ionizing orbital in this model. Again, its shape differs from that of the HOMO in the real benzene molecule which is odd with respect to reflection in the molecular plane and cannot be reproduced by the ZRP model. Recently, the ionization rates from several highest orbitals of the real benzene molecule have been calculated within the WFAT and used for the analysis of an experiment [20]. *Ab initio* coupled-cluster calculations for benzene were reported in Ref. [13].

Figure 7 shows the orientation dependence of the ionization rate. It is organized similarly to Fig. 2. The WFAT results shown in Fig. 7(a) reflect the shape of the ionizing orbital. The orbital has three nodal planes: the (x, z) plane and two planes obtained from it by rotations about the x axis by $\pm 60°$ (see Fig. 6). The nodal lines of G_{00} reflect these planes. The six maxima of $|G_{00}|^2$ correspond to orientations at which one of the hydrogen nuclei is located at the negative-z semiaxis and thus reflects the outer lobes of the orbital. The exact results for $F = 0.02$ shown in Fig. 7(b) qualitatively reproduce the maxima in the WFAT results, but do not fully reproduce valleys along the nodal lines of G_{00}. Moreover, their absolute values are by two orders of magnitude smaller than the WFAT results. Our calculations show that the WFAT
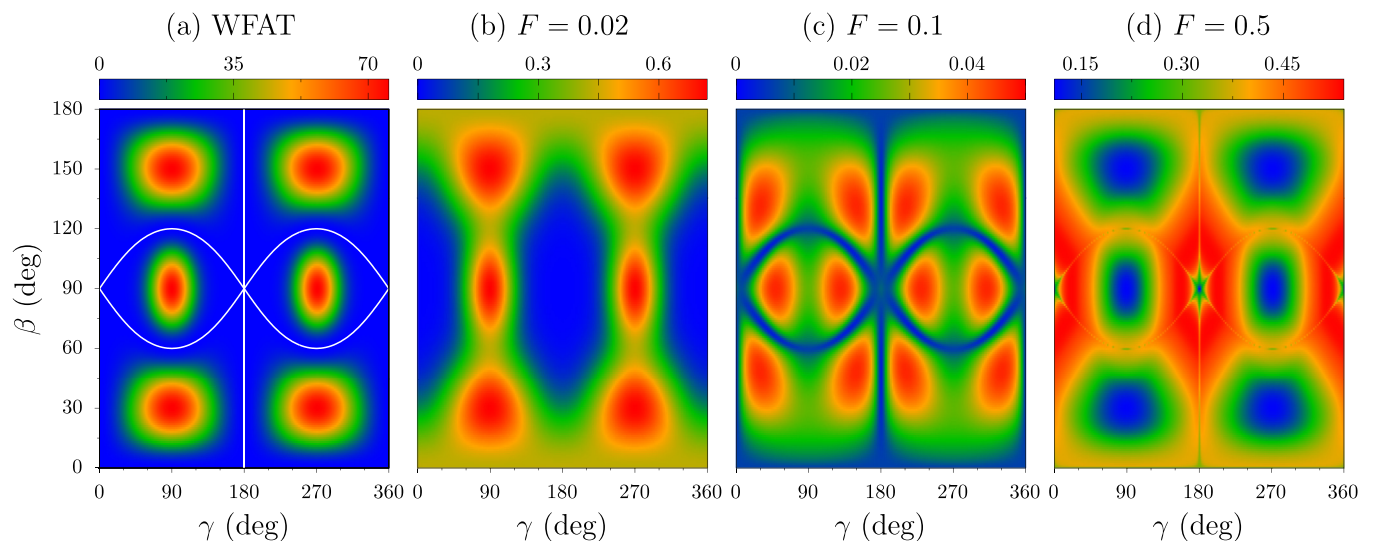

FIG. 7. The ratio Γ/W_{00}, similar to Fig. 2, but for the benzenelike molecule. The structure factor G_{00} turns to zero along the white lines in panel (a) and at its boundary. The values of the field factor are $W_{00} = 2.4 \times 10^{-11}$, 3.6×10^{-4}, and 3.6×10^{-2} for field strengths $F = 0.02$, 0.1, and 0.5, respectively.
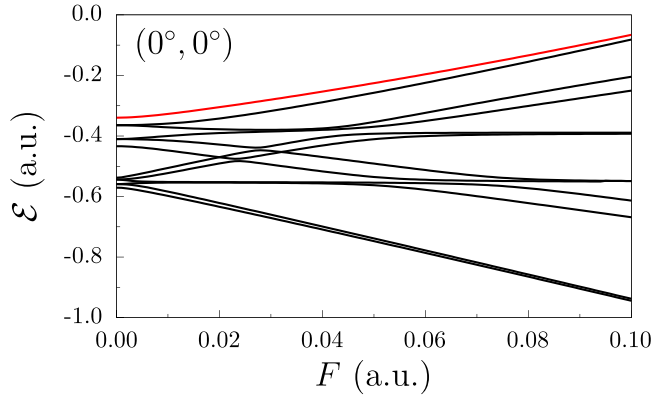
FIG. 8. Real parts of the energy eigenvalues (5) for 12 SSs originating from the bound states of the benzenelike molecule as functions of the field strength F at the orientation $(\beta, \gamma) = (0°, 0°)$. The top (red) line corresponds to the ionizing orbital.

does work quantitatively for the present molecule, but only at much weaker fields $F \lesssim 0.001$. The shapes of the results for stronger fields shown in Figs. 7(c) and 7(d) qualitatively differ not only from the predictions of the WFAT, but also from each other. In particular, each maximum in Figs. 7(a) and 7(b) is split into two maxima in Fig. 7(c) and then turns into a minimum in Fig. 7(d). This indicates that the restructuring of the ionizing orbital is happening more rapidly as the field grows than it was the case for the waterlike molecule.

Figure 8 explains this behavior. It shows the real parts of the exact energy eigenvalues for the SSs originating from the bound states of the system as functions of F at the orientation $(0°, 0°)$, similarly to the top panel in Fig. 3. The energies obtained from Eq. (52) are indistinguishable by eye from the exact results, so we use this equation to understand the dependence on F. The energies of the 12 unperturbed bound states at $F = 0$ lie in a narrow interval from $E_1 = -0.571$ to $E_{12} = -0.340$. States 2 and 3, 4 and 5, 8 and 9, and 10 and 11 are pairwise degenerate. This degeneracy is removed at $F > 0$. At weak fields the energies behave quadratically in F because all unperturbed states have zero dipoles. As the field grows, the term $F z_{nm}$ in Eq. (52) becomes dominant, and the energies begin to vary linearly in F. This results in many avoided crossings between the different states. The elements of the matrix z_{nm} are roughly speaking proportional to the size of the molecule. The present molecule is larger than the previous one, therefore, avoided crossings begin to appear at weaker fields. Note that the interval of F shown in Fig. 8 is smaller than that in Fig. 3. Although the ionizing state does not seem to pass through sharp avoided crossings in this interval at the orientation considered, it is strongly coupled to and mixed with the other states, and this results in the variation of the orientation dependence of the ionization rate seen in Fig. 7.

Figure 9 shows TMDs for two field strengths at four orientations of the molecule, similarly to Fig. 4. At orientations with $\gamma = 0°$ the SS eigenfunction is even with respect to
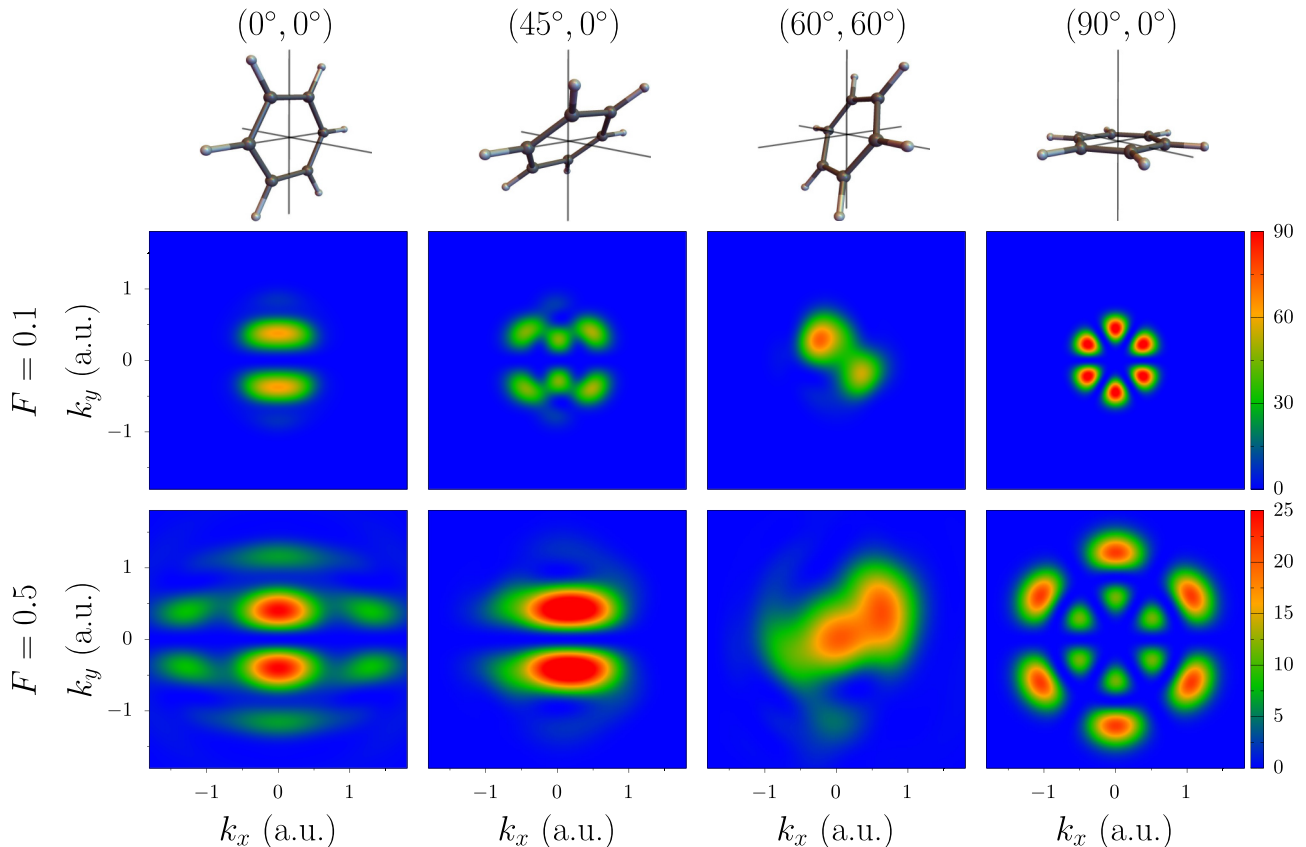

FIG. 9. The ratio $P(\mathbf{k}_\perp)/\Gamma$, similar to Fig. 3, but for the benzenelike molecule. The orientations (β, γ) of the molecule are indicated and illustrated in the top row.
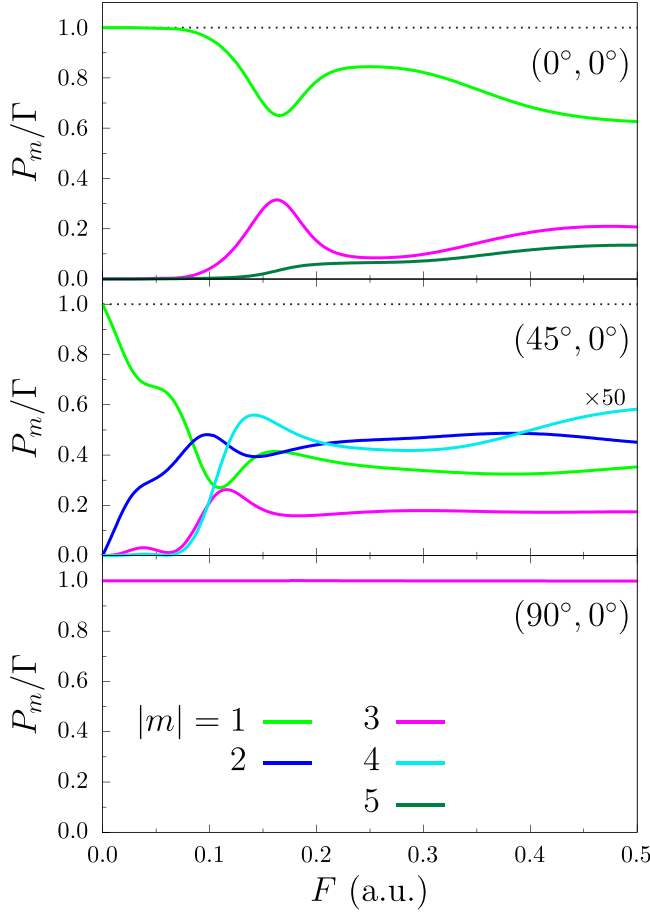
FIG. 10. Ratios P_m/Γ of partial ionization fluxes with $|m| > 0$ to the ionization rate for the benzenelike molecule as functions of the field strength F for three of the four orientations (β, γ) shown in Fig. 9. In all the cases $P_0 = 0$ and $P_{-|m|} = P_{|m|}$ for $|m| > 0$, so the lines show the sum $(P_{|m|} + P_{-|m|})/\Gamma$.

reflection $y \to -y$, therefore, the TMDs are symmetric with respect to $k_y \to -k_y$ and $P_{|m|} = P_{-|m|}$. Partial ionization fluxes for three such orientations from Fig. 9 as functions of F are shown in Fig. 10. In this case $P_0 = 0$ and the lines with $|m| > 0$ show the sum $(P_{|m|} + P_{-|m|})/\Gamma$. At the orientation $(\beta, \gamma) = (60°, 60°)$ this symmetry is broken, so $P_0 \neq 0$ and $P_{|m|} \neq P_{-|m|}$. Partial ionization fluxes for this orientation are shown in Fig. 11. In all the cases all fluxes visible on the scale of the figure are shown and Eq. (9) holds with an error less than 2.3%.

Consider the TMDs shown in Fig. 9 for the weaker field $F = 0.1$. In contrast to the case of the waterlike molecule, they do not have one of those basic shapes (62) or (63) predicted by the WFAT. Even the simplest of them, the TMD at the orientation $(0°, 0°)$, is formed by interfering contributions from four (taking into account the sign of m) channels with $|m| = 1$ and 3, as can be seen from the top panel in Fig. 10. The TMDs at orientations $(45°, 0°)$ and $(60°, 60°)$ reflect the interference of several channels with $|m| \leqslant 4$ (see the middle panel in Figs. 10 and 11). The most interesting is the TMD at the orientation $(90°, 0°)$. Here, because of the high symmetry of the SS eigenfunction, partial ionization fluxes with $|m| < 3$ are zero (see the bottom panel in Fig. 10). The TMD in this
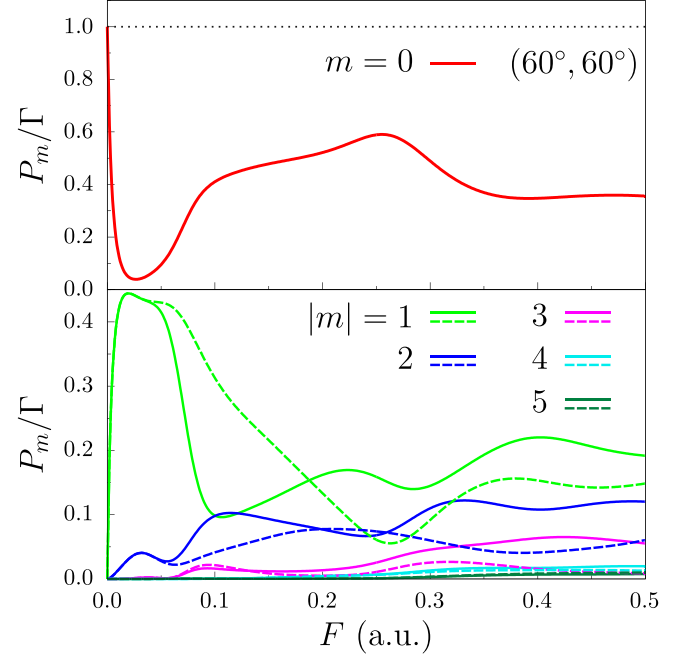
case is formed almost exclusively by channels with $|m| = 3$. For the stronger field $F = 0.5$, the number of channels giving comparable contributions to the total ionization flux becomes larger. As a result, the shapes of the TMDs become more complex, reflecting an interference of many channels with different m. Such TMDs encode structural information.

To illustrate the last point for the present molecule, let us analyze in more detail the shapes of the TMDs at the orientation $(90°, 0°)$ (see Fig. 9). In this case $R_{iz} = 0$ for all nuclei. Furthermore, the coefficients c_i for any two neighboring C or H nuclei differ only in sign (see Fig. 6), so there are only two independent coefficients c_C and c_H. Then Eq. (44) can be presented in the form

$$A(\mathbf{k}_\perp) = \frac{e^{i\pi/4}2\pi^{1/2}}{(2F)^{1/6}} \text{Ai}\left(\frac{k_\perp^2 - 2E}{(2F)^{2/3}}\right) \sum_{n=1}^{6} (-1)^n$$
$$\times (c_C e^{-i\mathbf{k}_\perp \mathbf{R}_{C_n}} + c_H e^{-i\mathbf{k}_\perp \mathbf{R}_{H_n}}), \quad (65)$$

where

$$\mathbf{R}_{A_n} = R_A(\cos[(1/2+n)\pi/3], \sin[(1/2+n)\pi/3], 0), \quad (66)$$

and the subscript A stands for either C or H. Substituting the expansion

$$e^{-i\mathbf{k}_\perp \mathbf{R}_{A_n}} = \sum_{m=-\infty}^{\infty} e^{-im(2+n)\pi/3} J_m(k_\perp R_A) e^{im\varphi_k} \quad (67)$$

and calculating the sum over n in Eq. (65), we obtain

$$A(\mathbf{k}_\perp) = \frac{24 e^{3i\pi/4} \pi^{1/2}}{(2F)^{1/6}} \text{Ai}\left(\frac{k_\perp^2 - 2E}{(2F)^{2/3}}\right) \sum_{M=0}^{\infty} [c_C J_{3+6M}(k_\perp R_C)$$
$$+ c_H J_{3+6M}(k_\perp R_H)] \sin[(3+6M)\varphi_k]. \quad (68)$$

FIG. 11. Ratios P_m/Γ of partial ionization fluxes to the ionization rate for the benzenelike molecule as functions of the field strength F for the third orientation $(\beta, \gamma) = (60°, 60°)$ from Fig. 9. Solid and dashed lines show the results for $m \geqslant 0$ and $m < 0$, respectively.

This representation of the TMD amplitude explains the shapes of $P(\mathbf{k}_\perp)$ for both field strengths at the present orientation shown in Fig. 9. In particular, the TMDs are invariant under the rotation $\varphi_k \to \varphi_k + \pi/3$. The Airy function in Eq. (68) decays as $k_\perp$ grows, so this factor acts as a window function determining the radius of the TMD in the $\mathbf{k}_\perp$ plane. In the weak-field limit this radius is $k_\perp \sim \sqrt{F/\varkappa}$ [see Eqs. (62) and (63)]; at stronger fields its dependence on F is less trivial, but it continues to grow with F. As follows from the bottom panel in Fig. 10, the main contribution to Eq. (68) comes from the term $M = 0$ which corresponds to $|m| = 3$ in Eq. (10). The next nonzero contribution comes from channels with $M = 1$, that is $|m| = 9$, which are not visible in Fig. 10. The number of maxima of the TMDs in the radial direction is determined by the interplay between the Airy factor and the Bessel functions. For the weaker field $F = 0.1$ the radius of the TMD is small, the Bessel functions can be replaced by their asymptotics at $k_\perp \to 0$, and hence there is only one radial maximum. For the stronger field $F = 0.5$ the radius becomes larger and the first oscillation of the Bessel functions becomes visible, which reveals the second radial maximum. Having thus decoded the structure of the TMD, we can extract from it the geometry of the molecule. We fit the exact TMD for $F = 0.5$ taken along the ray $\varphi_k = \pi/6$ by Eq. (68), where only one term with $M = 0$ is retained. In the fitting procedure we treat c_C, c_H, R_C, and R_H as free parameters. To introduce some additional uncertainty, we assume that the coefficients c_C and c_H are real. The geometrical parameters found from the fit are $(R_C)_{\text{fit}} = 2.477$ and $(R_H)_{\text{fit}} = 4.693$, which is very close to their exact values $R_C = 2.640$ and $R_H = 4.694$.

Summarizing, the size of the molecule matters, and for larger molecules all features noted in the conclusions of the previous subsection become more pronounced. Namely, avoided crossings causing qualitative modifications of the orientation dependence of the ionization rate begin to appear at weaker fields. The relative amount of vortex electrons with $|m| > 0$ generated in tunneling ionization and the largest $|m|$ contributing to the ionization flux at a given field grow. As a result, the interference structure of the TMD becomes richer.

C. Amino acid leucinelike molecule

As a final example we discuss a model of the leucine molecule $C_6H_{13}NO_2$ described by $N = 22$ ZRPs. This is a truly polyatomic molecule having no symmetry. The nuclear coordinates are taken from Ref. [82] and shifted by a common vector $\mathbf{a} = (-2, -2, 0)$ to place the geometric center of the molecule closer to the origin. The energy of the HOMO in the real leucine is $E_0 = -0.313$ [82,84]. The parameters $\varkappa_i$ are defined by Eq. (64), in the same way as in the previous subsection. The energy of the highest bound state in the ZRP model coincides with E_0 for $c = 0.999$, which gives $\varkappa_C = 0.909$, $\varkappa_H = 0.999$, $\varkappa_N = 1.033$, and $\varkappa_O = 1.000$. With these parameters the energy of the ground state is $E_1 = -0.617$.

Figure 12 shows the unperturbed ionizing orbital. Its shape indeed resembles a bunch of grapes. At zero field the coefficients c_i in Eq. (30) for several nuclei in the top part of the figure (including the nitrogen nucleus shown by the blue ball and both oxygen nuclei shown by red balls) are small, so the
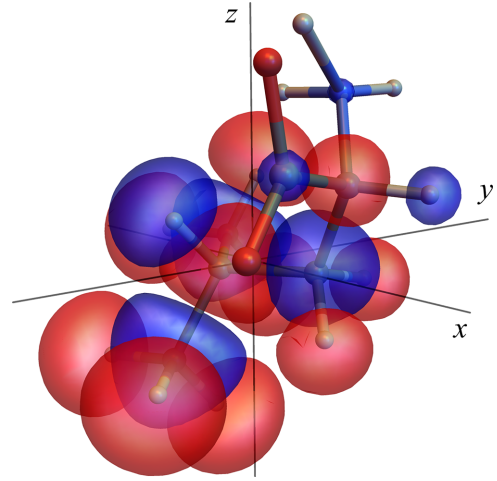

FIG. 12. The unperturbed ionizing orbital, similar to Figs. 1 and 6, but for the leucinelike molecule.

radii of the corresponding "grapes" are also small and they are not visible.

Figure 13 shows the orientation dependence of the ionization rate. The WFAT results are expected to reflect the shape of the ionizing orbital. Note, however, that here the shape in the asymptotic region is meant [see Eq. (59)], that is, the shape of an isosurface of $\phi_0(\mathbf{r})$ at an amplitude tending to zero. For the present molecule this shape differs considerably from that at a finite amplitude shown in Fig. 12. In particular, $\phi_0(\mathbf{r})$ has fewer nodal surfaces in the asymptotic region shown by white lines in Fig. 13(a) than would be expected from Fig. 12, which means that some nodal surfaces are closed. In contrast to previous molecules, WFAT reproduces neither the shape nor the absolute values of the exact results even for the weakest field considered $F = 0.02$. A new feature compared to Figs. 2 and 13 is the appearance of lines across which the ionization rate varies very rapidly, almost discontinuously. As seen from Figs. 13(b)–13(d), the density of such lines in the (β, γ) plane grows with the field.

Figure 14 explains the origin of the apparent discontinuities. It shows the difference $\mathcal{E}_{22} - \mathcal{E}_{21}$ between the two highest eigenvalues of Eq. (52) as a function of the orientation angles (β, γ) for two stronger fields from Fig. 13. The net of blue lines in the figure indicates the locations of sharp avoided crossings. These avoided crossings cause the rapid variation of Γ seen in Fig. 13. The present molecule illustrates that such avoided crossings can be encountered not only when changing the field strength, but also the molecular orientation. The fact that they are distributed more densely for stronger fields is explained by large values of the elements of the dipole matrix (53) reflecting the large size of the molecule.

Figure 15 shows TMDs for two field strengths at four representative orientations. Even for the weaker field $F = 0.1$ the shapes of the TMDs are far from the basic shapes (62) and (63) predicted by the WFAT. For the stronger field $F = 0.5$ the TMDs show a very rich interference structure. Partial ionization fluxes for the same orientations as functions of F are shown in Fig. 16 for plane-wave electrons with $m = 0$ and Fig. 17 for vortex electrons with $|m| > 0$. The present molecule does not have any symmetry, so $P_{|m|}$ and $P_{-|m|}$ are
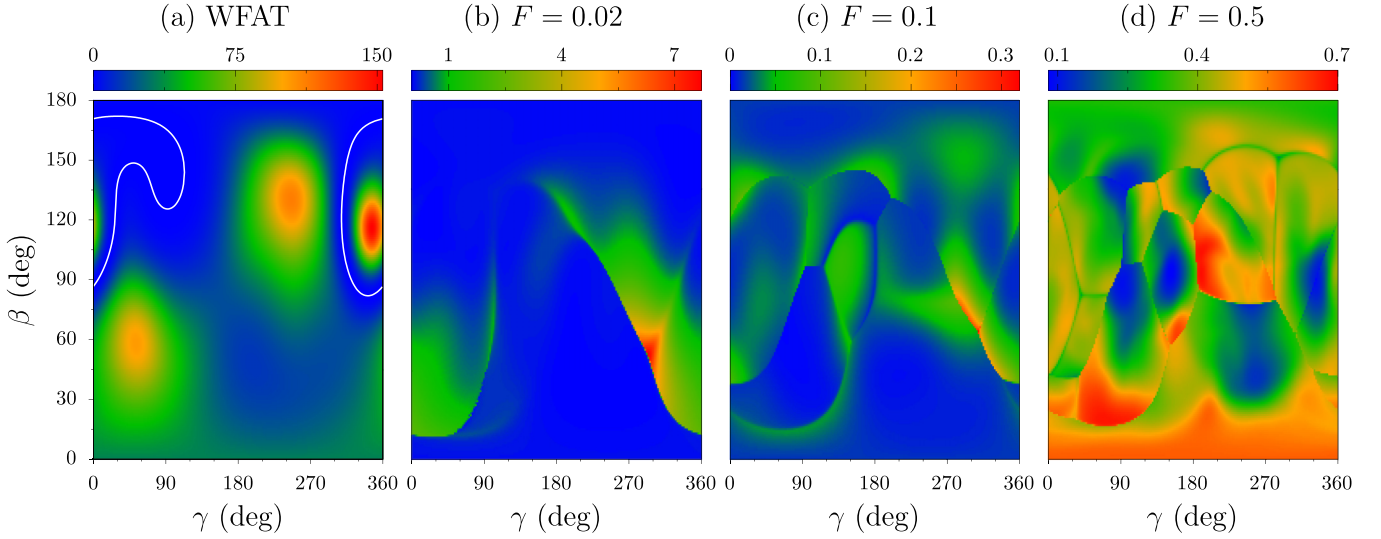
FIG. 13. The ratio Γ/W_{00}, similar to Figs. 2 and 7, but for the leucinelike molecule. The values of the field factor are $W_{00} = 2.2 \times 10^{-10}$, 5.9×10^{-4}, and 4.1×10^{-2} for field strengths $F = 0.02$, 0.1, and 0.5, respectively.

different and the difference is seen to grow with F. These results confirm previous conclusions: for larger molecules the relative role of the contributions from channels with $|m| > 0$ to the total ionization flux as well as the maximum $|m|$ present in the flux become larger, and this abundance of vortex electrons results in the complex structure of the TMD.

D. Tunneling-induced electron diffraction

It is instructive to look at the TMD from a different perspective. Suppose an electron is localized in the top part of a large molecule extended along the field. If the field is sufficiently strong, so that the tunneling exit is located inside the molecule, then before leaving the molecule the electron can be scattered by nuclei in its bottom part. We call this process tunneling-induced electron diffraction. It is similar to the x-ray photoelectron diffraction [85], but the diffracting
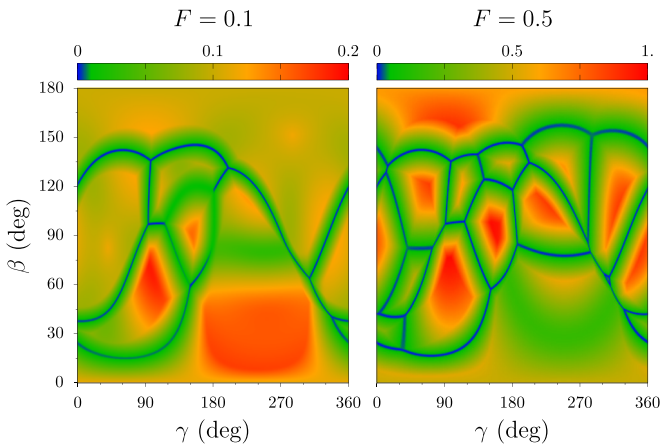

FIG. 14. The difference between the two highest eigenvalues of Eq. (52) for the leucinelike molecule as a function of the orientation angles (β, γ) for two field strengths F indicated in the figure. The blue lines indicate the locations of sharp avoided crossings.

electron is released by tunneling rather than absorption of a photon. Let us show that the TMD encodes information about such diffraction.

Consider tunneling ionization from the upper state in a homonuclear diatomic molecule described by two ZRPs located at $\mathbf{R}_\pm = (0, 0, \pm R)$ characterized by a parameter $\varkappa$. To simplify the analysis and make its result most transparent, we consider the asymptotics

$$F \to 0, \quad R = O(F^{-1}). \tag{69}$$

In this case the ionizing state is localized near the upper nucleus at $\mathbf{R}_+$. Its energy can be obtained from Eq. (34) by neglecting the presence of the lower nucleus at $\mathbf{R}_-$,

$$\frac{\varkappa}{2\pi} + G_{\mathrm{reg}}(\mathbf{R}_+; E) = 0 \; \to \; E \approx -\frac{\varkappa^2}{2} + FR + O(F^2). \tag{70}$$

The SS eigenfunction (30) has the form

$$\phi(\mathbf{r}) = c_+ G(\mathbf{r}, \mathbf{R}_+; E) + c_- G(\mathbf{r}, \mathbf{R}_-; E). \tag{71}$$

Using Eq. (32), the coefficient c_- can be expressed in terms of c_+,

$$c_- \approx -\frac{G(\mathbf{R}_-, \mathbf{R}_+; E)}{\frac{\varkappa}{2\pi} + G_{\mathrm{reg}}(\mathbf{R}_-; E)} c_+. \tag{72}$$

Consider the function (71) in the region $r' = O(F^0)$, where $\mathbf{r}' = \mathbf{r} - \mathbf{R}_-$. We substitute E from Eq. (70). In the same approximation $c_+ = \sqrt{2\pi\varkappa}$. By expanding in F we obtain

$$\phi(\mathbf{r}) = \frac{e^{i\pi/4}}{4R} \frac{\varkappa - ik_{\mathrm{in}}}{\sqrt{2\pi k_{\mathrm{in}}}} \exp\left(\frac{ik_{\mathrm{in}}^3 - \varkappa^3}{3F}\right)$$

$$\times \left[e^{-ik_{\mathrm{in}}z'} + f(k_{\mathrm{in}}) \frac{e^{ik_{\mathrm{in}}r'}}{r'} \right], \tag{73}$$
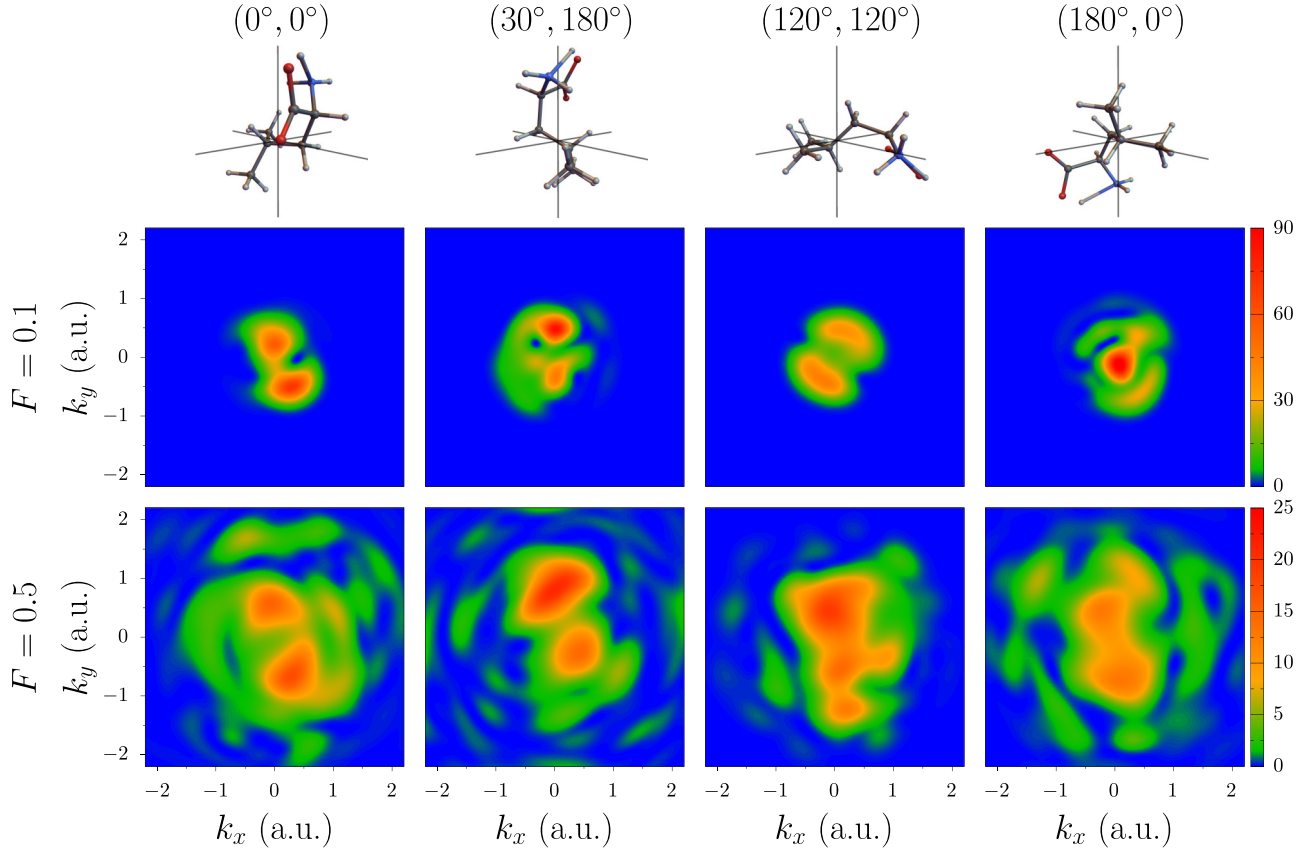
FIG. 15. The ratio $P(\mathbf{k}_\perp)/\Gamma$, similar to Figs. 3 and 8, but for the leucinelike molecule. The orientations (β, γ) of the molecule are indicated and illustrated in the top row.

where $k_{\text{in}} = \sqrt{4FR - \varkappa^2}$ and

$$f(k) = \frac{-1}{\varkappa + ik}. \tag{74}$$

The function in the square brackets in Eq. (73) is the scattering state in the lower ZRP with the incident momentum $\mathbf{k}_{\text{in}} = (0, 0, -k_{\text{in}})$ and $f(k_{\text{in}})$ is the corresponding elastic scattering amplitude [21]. The incident and scattered waves in this function originate from the first and second terms in Eq. (71), respectively. Under the same approximations the TMD amplitude (44) is given by

$$A(\mathbf{k}_\perp) = e^{i\pi/4}\sqrt{2\pi}\exp\left(-\frac{\varkappa^3}{3F}\right)\Bigg[\exp\left(-\frac{\varkappa k_\perp^2}{2F}\right)$$
$$+ \frac{e^{ik_{\text{in}}^3/3F + i\pi/4}\pi^{1/2}(\varkappa - ik_{\text{in}})}{2R(2F)^{1/6}k_{\text{in}}^{1/2}}f(k_{\text{in}})\text{Ai}\left(\frac{k_\perp^2 - k_{\text{in}}^2}{(2F)^{2/3}}\right)\Bigg], \tag{75}$$

where the two terms in the square brackets originate from the corresponding terms in Eqs. (71) and (73). Equation (73) supports the following picture of the ionization dynamics in the present model. The tunneling exit is defined by $E = Fz_t$, thus $z_t = R - \varkappa^2/2F$. It is located above the lower nucleus if $z_t > -R$, that is, $4FR > \varkappa^2$. In this case the electron after tunneling is accelerated by the field and arrives at the lower nucleus with momentum $\mathbf{k}_{\text{in}}$. Thus, the maximum value of its transverse momentum after scattering is k_{in}. This agrees with

Eq. (75). Indeed, the first term in this equation is the TMD amplitude for electrons liberated from the upper center, as if there was no lower nucleus [compare with the first term in Eq. (61)]. The second term originates from scattering by the lower nucleus. The Airy function in this term rapidly decays at $k_\perp > k_{\text{in}}$, which confirms the above picture.

Figure 18 shows the exact TMD for the present model with $R = 3.5$ and $\varkappa = 1$ calculated for $F = 0.5$ using Eq. (44). In this case $k_{\text{in}} = 2.45$. The present potential is axially symmetric about the z axis, so the TMD does not depend on φ_k and is denoted by $P(k_\perp)$. The solid black line shows the total TMD. Dashed red and blue lines are obtained by retaining in Eq. (44) only one term corresponding to the upper and lower nucleus, respectively. The contribution from the upper nucleus $P_+(k_\perp)$ monotonically decays, while that from the lower nucleus $P_-(k_\perp)$ oscillates at $k_\perp < k_{\text{in}}$ and decays at $k_\perp > k_{\text{in}}$. All this qualitatively agrees with the behavior predicted by the asymptotics (75).

Let us use this model to identify traces of tunneling-induced electron diffraction in TMDs discussed above. Consider the TMD for the leucinelike molecule at $F = 0.5$ and $(\beta, \gamma) = (30°, 180°)$ shown in Fig. 15. At this orientation the molecule is aligned along the field and we expect that it can be approximately described by the model. The dashed-dotted green line in Fig. 18 shows the TMD averaged over φ_k. One can clearly see a maximum at $k_\perp \approx 2.25$ corresponding to the concentric circular structures in Fig. 15 whose position and height are well reproduced by the model. Note that the
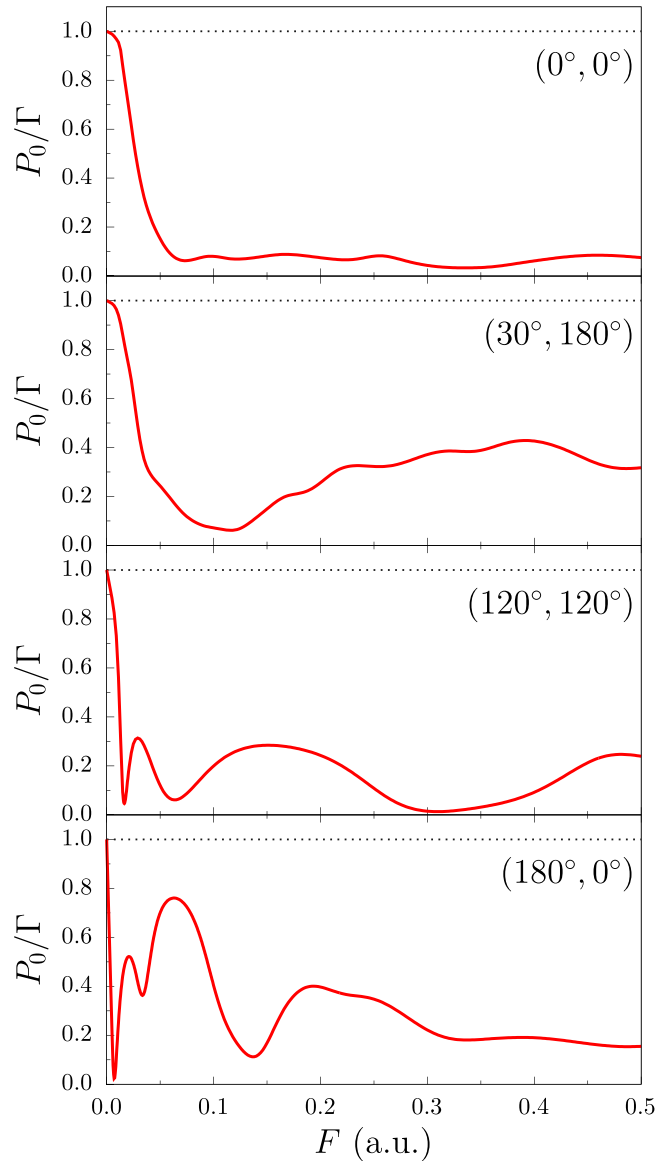
FIG. 16. Ratios P_0/Γ of partial ionization fluxes with $m = 0$ to the ionization rate for the leucinelike molecule as functions of the field strength F for the same four orientations (β, γ) as in Fig. 15.

FIG. 17. Ratios P_m/Γ for the leucinelike molecule, similar to Fig. 16, but for $|m| > 0$. Solid and dashed lines show the results for $m > 0$ and $m < 0$, respectively.

distance between the top and bottom nuclei in the leucinelike molecule at this orientation is about 11, which gives $R \approx 5.5$. The difference between this value and $R = 3.5$ used in the model as well as that between the solid and dashed-dotted lines in Fig. 18 at smaller $k_\perp$ are explained by the fact that the ionizing state is not perfectly localized at one nucleus in the top part of the molecule and there is more than one nucleus in its bottom part on which tunneled electrons can scatter. Nevertheless, in spite of the differences, this comparison suggests that circular structures in the outer part of TMDs for the leucinelike molecule shown in Fig. 15 result from the tunneling-induced diffraction mechanism.

VII. CONCLUSIONS AND OUTLOOK

In this paper, we have extended the zero-range potential model for molecules from studies of bound states [21,22]
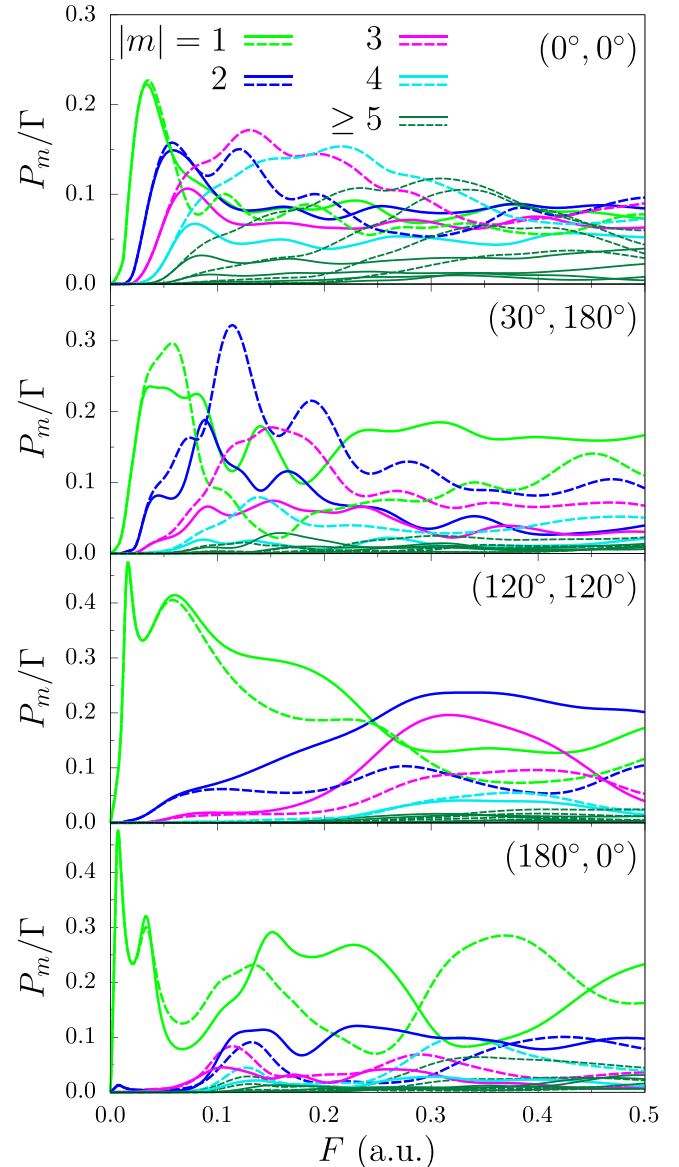
to the analysis of Siegert states in an electric field [3–5,14]. The recently derived closed-form expression for the outgoing-wave Green's function for an electron in a homogeneous static electric field [55,56] greatly facilitates the analysis. Simple analytical equations defining the Siegert states are obtained, which makes virtually exact calculation of tunneling ionization observables for large polyatomic molecules with complex geometry in strong fields possible. The theory is illustrated by calculations for three model molecules reproducing the geometry of the real water, benzene, and leucine molecules. The exact results are compared with the predictions of the weak-field asymptotic theory [14]. We have discussed the field and orientation dependence of not only the ionization rate, which is usually of main interest for applications in strong-filed physics [1], but also the transverse momentum distribution of liberated electrons, which defines the photo-
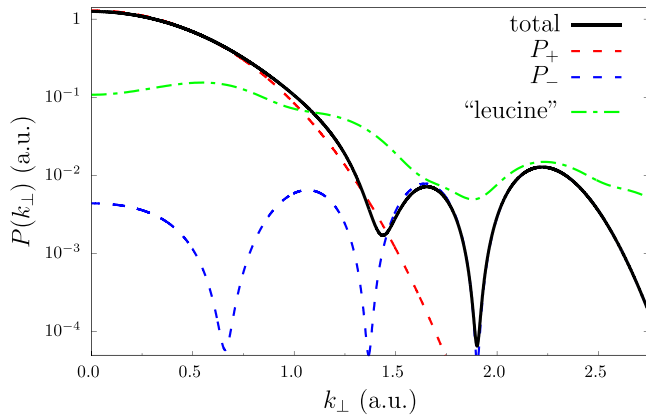
FIG. 18. The solid black line shows the total TMD for a diatomic molecule with $R = 3.5$ and $\varkappa = 1$ calculated for $F = 0.5$ using Eq. (44). Dashed red (P_+) and blue (P_-) lines are obtained by retaining in Eq. (44) only one term corresponding to the upper and lower nucleus, respectively. The dashed-dotted green line is obtained by averaging the TMD for the leucinelike molecule at $F = 0.5$ and $(\beta, \gamma) = (30°, 180°)$ (see Fig. 15) over φ_k.

electron momentum distribution resulting from strong-field ionization in the adiabatic regime [2], with a focus on the generation of vortex electrons. Our main conclusions supported by the calculations can be summarized as follows. First, it is well known that in the weak-field limit the orientation dependence of the ionization rate reproduces the shape of the unperturbed ionizing orbital [67–72]. It is also known that the orbital is distorted as the field grows and this distortion is reflected in the ionization rate [73–80]. The present results show that as the field grows further, the ionizing orbital may undergo restructuring due to avoided crossings with other states, which leads to a qualitative modification of the orientation dependence of the ionization rate. Second, while at weak fields tunneling ionization is dominated by plane-wave electrons having zero projection m of their angular momentum on the field [14], at stronger fields contributions from vortex electrons with $|m| > 0$ grow and become comparable to that from $m = 0$ and the largest $|m|$ present in the ionization flux also grows. In other words, vortex electrons are efficiently generated in the tunneling ionization process. Third, the transverse momentum distribution, which at weak fields

has a simple Gaussian shape [14], at stronger fields acquires a complex structure resulting from the interference of many vortex channels. We have shown that this structure encodes information about the geometry of the molecule. Furthermore, we have described tunneling-induced electron diffraction and showed that under certain conditions it is manifested in the shape of the transverse momentum distribution. Finally, for large polyatomic molecules such as amino acids all the effects indicated above become more pronounced and begin to appear at weaker fields.

Let us mention one of the most promising prospects opened by this study. Recently, the adiabatic theory of generation and rescattering of vortex electrons by strong-field ionization from a vortex orbital in a linear molecule aligned along the laser field has been developed [44,45]. Since scattering of vortex electrons by a chiral molecular ion is an enantiosensitive process, this theory suggests that extending rescattering photoelectron spectroscopy [46–53] to vortex electrons will provide access to probing molecular chirality. The present results show that vortex electrons are generated in abundance in tunneling ionization of large molecules without any symmetry at sufficiently strong fields, which is a prerequisite for enantiosensitive rescattering spectroscopy. At the same time, the present model enables one to implement the theory of Refs. [44,45] for large chiral molecules and thus to quantitatively analyze the enantiosensitivity. A work in this direction is in progress.

Although in this paper we treated tunneling ionization in a static electric field, the results obtained are of main interest for the analysis of strong-field ionization by intense laser pulses on the basis of the adiabatic theory [2]. This theory becomes exact as the laser wavelength tends to infinity. Its good quantitative performance for realistic laser pulses was demonstrated by comparison with numerical solution of the time-dependent Schrödinger equation [2,44,49]. In particular, for laser wavelength $\sim$800 nm and intensity $\sim$3$\times$10^{14} W/cm^2 its error in predicting photoelectron momentum distribution near a backward rescattering caustic, which is measured in rescattering photoelectron spectroscopy, does not exceed a few percent [44,49].

ACKNOWLEDGMENT

[1] F. Krausz and M. Ivanov, Attosecond physics, Rev. Mod. Phys. **81**, 163 (2009).

[2] O. I. Tolstikhin and T. Morishita, Adiabatic theory of ionization by intense laser pulses: Finite-range potentials, Phys. Rev. A **86**, 043417 (2012).

[3] P. A. Batishchev, O. I. Tolstikhin, and T. Morishita, Atomic Siegert states in an electric field: Transverse momentum distribution of the ionized electrons, Phys. Rev. A **82**, 023416 (2010).

[4] L. Hamonou, T. Morishita, and O. I. Tolstikhin, Molecular Siegert states in an electric field, Phys. Rev. A **86**, 013412 (2012).

[5] V. N. T. Pham, O. I. Tolstikhin, and T. Morishita, Molecular Siegert states in an electric field. II. Transverse momentum distribution of the ionized electrons, Phys. Rev. A **89**, 033426 (2014).

[6] M. Z. Milošević and N. S. Simonović, Calculations of rates for strong-field ionization of alkali-metal atoms in the quasistatic regime, Phys. Rev. A **91**, 023424 (2015).

[7] I. I. Fabrikant and L. B. Zhao, Green-function approach to the theory of tunneling ionization, Phys. Rev. A **91**, 053412 (2015).

[8] P. Pirkola and M. Horbatsch, Partial-wave approach to the Stark resonance problem of the water molecule, Phys. Rev. A **105**, 032814 (2022).

[9] P. Pirkola and M. Horbatsch, Calculation of DC Stark resonances for the ammonia molecule, Molecules **29**, 1543 (2024).

[10] V. P. Majety and A. Scrinzi, Static field ionization rates for multi-electron atoms and small molecules, J. Phys. B: At. Mol. Opt. Phys. **48**, 245603 (2015).

[11] T.-C. Jagau, Coupled-cluster treatment of molecular strong-field ionization, J. Chem. Phys. **148**, 204102 (2018).

[12] M. Hernández Vera and T.-C. Jagau, Resolution-of-the-identity approximation for complex-scaled basis functions, J. Chem. Phys. **151**, 111101 (2019).

[13] M. Hernández Vera and T.-C. Jagau, Resolution-of-the-identity second-order Møller-Plesset perturbation theory with complex basis functions: Benchmark calculations and applications to strong-field ionization of polyacenes, J. Chem. Phys. **152**, 174103 (2020).

[14] O. I. Tolstikhin, T. Morishita, and L. B. Madsen, Theory of tunneling ionization of molecules: Weak-field asymptotics including dipole effects, Phys. Rev. A **84**, 053423 (2011).

[15] O. I. Tolstikhin, L. B. Madsen, and T. Morishita, Weak-field asymptotic theory of tunneling ionization in many-electron atomic and molecular systems, Phys. Rev. A **89**, 013421 (2014).

[16] A. I. Dnestryan, O. I. Tolstikhin, L. B. Madsen, and F. Jensen, Structure factors for tunneling ionization rates of molecules: General grid-based methodology and convergence studies, J. Chem. Phys. **149**, 164107 (2018).

[17] I. S. Wahyutama, D. D. Jayasinghe, F. Mauger, K. Lopata, M. B. Gaarde, and K. J. Schafer, All-electron, density-functional-based method for angle-resolved tunneling ionization in the adiabatic regime, Phys. Rev. A **106**, 052211 (2022).

[18] S. Song, M. Zhu, H. Ni, and J. Wu, PyStructurefactor: A Python code for the molecular structure factor in tunneling ionization rates, Comput. Phys. Commun. **292**, 108882 (2023).

[19] A. I. Dnestryan, O. I. Tolstikhin, F. Jensen, and L. B. Madsen, Torsional effects in strong-field ionization of molecules, Phys. Rev. Res. **1**, 023018 (2019).

[20] A. Tehlar, J. T. Casanova, A. Dnestryan, F. Jensen, L. B. Madsen, O. I. Tolstikhin, and H. J. Wörner, High-harmonic spectroscopy of impulsively aligned 1,3-cyclohexadiene: Signatures of attosecond charge migration, Struct. Dyn. **11**, 014304 (2024).

[21] Y. N. Demkov and V. N. Ostrovskii, *Zero-Range Potentials and Their Applications in Atomic Physics* (Plenum, New York, 1988).

[22] G. Drukarev, *The Zero-range Potential Model and Its Application in Atomic and Molecular Physics* (Academic Press, New York, 1978), pp. 251–274.

[23] Y. N. Demkov and G. F. Drukarev, Decay and polarizability of a negative ion in an electric field, Zh. Eksp. Teor. Fiz. **47**, 918 (1964) [Sov. Phys. JETP **20**, 614 (1965)].

[24] F. I. Dalidchik and V. Z. Slonim, Strong exchange interaction effects in a homogeneous electric field, Zh. Eksp. Teor. Fiz. **70**, 47 (1976) [Sov. Phys. JETP **43**, 25 (1976)].

[25] S. V. Borzunov, N. L. Manakov, A. F. Starace, and M. V. Frolov, Decay of a negative molecular ion in a constant electric field, Zh. Eksp. Teor. Fiz. **139**, 835 (2011) [Sov. Phys. JETP **112**, 725 (2011)].

[26] N. L. Manakov and L. P. Rapoport, Particle with low binding energy in a circularly polarized field, Zh. Eksp. Teor. Fiz. **69**, 842 (1975) [Sov. Phys. JETP **42**, 430 (1975)].

[27] I. J. Berson, Multiphoton ionization and stimulated bremsstrahlung radiation in the case of short-range potentials, J. Phys. B: At. Mol. Phys. **8**, 3078 (1975).

[28] G. Alvarez and B. Sundaram, Perturbation theory for Floquet eigenvalues in a zero-range potential, Phys. Rev. A **42**, 452 (1990).

[29] W. Becker, S. Long, and J. K. McIver, Short-range potential model for multiphoton detachment of the H^- ion, Phys. Rev. A **42**, 4416 (1990).

[30] P. S. Krstić, D. B. Milosević, and R. K. Janev, Zero-range potential model for the description of atomic and molecular systems in a laser field, Phys. Rev. A **44**, 3089 (1991).

[31] W. Becker, S. Long, and J. K. McIver, Modeling harmonic generation by a zero-range potential, Phys. Rev. A **50**, 1540 (1994).

[32] J. Z. Kamiński, Stabilization and the zero-range models, Phys. Rev. A **52**, 4976 (1995).

[33] G. F. Gribakin and M. Y. Kuchiev, Multiphoton detachment of electrons from negative ions, Phys. Rev. A **55**, 3760 (1997).

[34] M. V. Frolov, N. L. Manakov, E. A. Pronin, and A. F. Starace, Model-independent quantum approach for intense laser detachment of a weakly bound electron, Phys. Rev. Lett. **91**, 053003 (2003).

[35] A. Gazibegović-Busuladžić, D. B. Milošević, and W. Becker, High-energy above-threshold detachment from negative ions, Phys. Rev. A **70**, 053403 (2004).

[36] A. S. Baltenkov, V. K. Dolmatov, S. T. Manson, and A. Z. Msezane, Nondipole effects in the photoabsorption of electrons in two-centre zero-range potentials, J. Phys. B: At. Mol. Opt. Phys. **37**, 3837 (2004).

[37] C. Arendt, D. Dimitrovski, and J. S. Briggs, Electron detachment from negative ions by few-cycle laser pulses: Dependence on pulse duration, Phys. Rev. A **76**, 023423 (2007).

[38] M. V. Frolov, N. L. Manakov, and A. F. Starace, Analytic formulas for above-threshold ionization or detachment plateau spectra, Phys. Rev. A **79**, 033406 (2009).

[39] W. Becker and D. Milošević, Multiphoton detachment from a zero-range potential revisited, Opt. Commun. **283**, 850 (2010).

[40] S. V. Borzunov, M. V. Frolov, M. Y. Ivanov, N. L. Manakov, S. S. Marmo, and A. F. Starace, Zero-range-potential model for strong-field molecular processes: Dynamic polarizability and photodetachment cross section, Phys. Rev. A **88**, 033410 (2013).

[41] V. M. Rylyuk, Enhancement of strong-electromagnetic-field ionization in a constant magnetic field, Phys. Rev. A **100**, 053409 (2019).

[42] W. Becker, F. Grasbon, R. Kopold, D. Milošević, G. Paulus, and H. Walther, *Above-threshold Ionization: From Classical Features to Quantum Effects* (Academic Press, New York, 2002), pp. 35–98.

[43] N. L. Manakov, M. V. Frolov, B. Borca, and A. F. Starace, Multiphoton detachment of a negative ion by an elliptically polarized, monochromatic laser field, J. Phys. B: At. Mol. Opt. Phys. **36**, R49 (2003).

[44] O. I. Tolstikhin and T. Morishita, Strong-field ionization, rescattering, and target structure imaging with vortex electrons, Phys. Rev. A **99**, 063415 (2019).

[45] K. V. Bazarov and O. I. Tolstikhin, Adiabatic theory of generation and rescattering of vortex electrons in strong-field

ionization by elliptically polarized pulses, Phys. Rev. A **107**, 053114 (2023).

[46] T. Morishita, A.-T. Le, Z. Chen, and C. D. Lin, Accurate retrieval of structural information from laser-induced photoelectron and high-order harmonic spectra by few-cycle laser pulses, Phys. Rev. Lett. **100**, 013903 (2008).

[47] M. Okunishi, T. Morishita, G. Prümper, K. Shimada, C. D. Lin, S. Watanabe, and K. Ueda, Experimental retrieval of target structure information from laser-induced rescattered photoelectron momentum distributions, Phys. Rev. Lett. **100**, 143001 (2008).

[48] D. Ray, B. Ulrich, I. Bocharova, C. Maharjan, P. Ranitovic, B. Gramkow, M. Magrakvelidze, S. De, I. V. Litvinyuk, A. T. Le, T. Morishita, C. D. Lin, G. G. Paulus, and C. L. Cocke, Large-angle electron diffraction structure in laser-induced rescattering from rare gases, Phys. Rev. Lett. **100**, 143002 (2008).

[49] T. Morishita and O. I. Tolstikhin, Adiabatic theory of strong-field photoelectron momentum distributions near a backward rescattering caustic, Phys. Rev. A **96**, 053416 (2017).

[50] Y. Ito, M. Okunishi, T. Morishita, O. I. Tolstikhin, and K. Ueda, Rescattering photoelectron spectroscopy of heterodiatomic molecules with an analytical returning photoelectron wave packet, Phys. Rev. A **97**, 053411 (2018).

[51] M. Okunishi, Y. Ito, V. Sharma, S. Aktar, K. Ueda, R. R. Lucchese, A. I. Dnestryan, O. I. Tolstikhin, S. Inoue, H. Matsui, and T. Morishita, Rescattering photoelectron spectroscopy of the CO_2 molecule: Progress towards experimental discrimination between theoretical target-structure models, Phys. Rev. A **100**, 053404 (2019).

[52] T. Mizuno, N. Ishii, T. Kanai, P. Rosenberger, D. Zietlow, M. F. Kling, O. I. Tolstikhin, T. Morishita, and J. Itatani, Observation of the quantum shift of a backward rescattering caustic by carrier-envelope phase mapping, Phys. Rev. A **103**, 043121 (2021).

[53] T. Mizuno, T. Yang, T. Kurihara, N. Ishii, T. Kanai, O. I. Tolstikhin, T. Morishita, and J. Itatani, Comparative study of photoelectron momentum distributions from Kr and CO_2 near a backward rescattering caustic by carrier-envelope-phase mapping, Phys. Rev. A **107**, 033101 (2023).

[54] R. P. Feynman and A. R. Hibbs, *Quantum Mechanics and Path Integrals* (McGraw-Hill, New York, 1965).

[55] A. V. Flegel, Integral representations for products of Airy functions and their application for analysis of the Green's function for a particle in a uniform static field, J. Phys. A: Math. Theor. **56**, 495304 (2023).

[56] K. V. Bazarov and O. I. Tolstikhin, Integral representations for products of two solutions of the Airy equation with shifted arguments and their applications in physics, Z. Angew. Math. Phys. **75**, 72 (2024).

[57] M. Abramowitz and I. A. Stegun, *Handbook of Mathematical Functions with Formulas, Graphs, and Mathematical Tables* (Dover, New York, 1964).

[58] R. G. Newton, *Scattering Theory of Waves and Particles* (Springer, New York, 1982).

[59] N. Dunford and J. T. Schwartz, *Linear Operators, Part 1: General Theory* (Wiley, Hoboken, NJ, 1988).

[60] A. V. Gets and O. I. Tolstikhin, Static-field-induced states, Phys. Rev. A **87**, 013419 (2013).

[61] V. H. Trinh, O. I. Tolstikhin, L. B. Madsen, and T. Morishita, First-order correction terms in the weak-field asymptotic theory of tunneling ionization, Phys. Rev. A **87**, 043426 (2013).

[62] A. I. Dnestryan and O. I. Tolstikhin, Integral-equation approach to the weak-field asymptotic theory of tunneling ionization, Phys. Rev. A **93**, 033412 (2016).

[63] P. K. Samygin, T. Morishita, and O. I. Tolstikhin, Weak-field asymptotic theory of tunneling ionization from nearly degenerate states, Phys. Rev. A **98**, 033401 (2018).

[64] A. R. Edmonds, *Angular Momentum in Quantum Mechanics* (Princeton University Press, Princeton, NJ, 1957).

[65] L. B. Madsen, O. I. Tolstikhin, and T. Morishita, Application of the weak-field asymptotic theory to the analysis of tunneling ionization of linear molecules, Phys. Rev. A **85**, 053404 (2012).

[66] L. B. Madsen, F. Jensen, O. I. Tolstikhin, and T. Morishita, Application of the weak-field asymptotic theory to tunneling ionization of H_2 O, Phys. Rev. A **89**, 033412 (2014).

[67] D. Pavičić, K. F. Lee, D. M. Rayner, P. B. Corkum, and D. M. Villeneuve, Direct measurement of the angular dependence of ionization for N_2, O_2, and CO_2 in intense laser fields, Phys. Rev. Lett. **98**, 243001 (2007).

[68] H. Akagi, T. Otobe, A. Staudte, A. Shiner, F. Turner, R. Dörner, D. M. Villeneuve, and P. B. Corkum, Laser tunnel ionization from multiple orbitals in HCl, Science **325**, 1364 (2009).

[69] A. Staudte, S. Patchkovskii, D. Pavičić, H. Akagi, O. Smirnova, D. Zeidler, M. Meckel, D. M. Villeneuve, R. Dörner, M. Y. Ivanov, and P. B. Corkum, Angular tunneling ionization probability of fixed-in-space H_2 molecules in intense laser pulses, Phys. Rev. Lett. **102**, 033004 (2009).

[70] J. Wu, L. P. H. Schmidt, M. Kunitski, M. Meckel, S. Voss, H. Sann, H. Kim, T. Jahnke, A. Czasch, and R. Dörner, Multiorbital tunneling ionization of the CO molecule, Phys. Rev. Lett. **108**, 183001 (2012).

[71] J. L. Hansen, L. Holmegaard, J. H. Nielsen, H. Stapelfeldt, D. Dimitrovski, and L. B. Madsen, Orientation-dependent ionization yields from strong-field ionization of fixed-in-space linear and asymmetric top molecules, J. Phys. B: At. Mol. Opt. Phys. **45**, 015101 (2012).

[72] J. Yao, G. Li, X. Jia, X. Hao, B. Zeng, C. Jing, W. Chu, J. Ni, H. Zhang, H. Xie, C. Zhang, Z. Zhao, J. Chen, X. Liu, Y. Cheng, and Z. Xu, Alignment-dependent fluorescence emission induced by tunnel ionization of carbon dioxide from lower-lying orbitals, Phys. Rev. Lett. **111**, 133001 (2013).

[73] G. Lagmago Kamta and A. D. Bandrauk, Imaging electron molecular orbitals via ionization by intense femtosecond pulses, Phys. Rev. A **74**, 033415 (2006).

[74] M. Abu-samha and L. B. Madsen, Theory of strong-field ionization of aligned CO_2, Phys. Rev. A **80**, 023401 (2009).

[75] S.-K. Son and S.-I. Chu, Multielectron effects on the orientation dependence and photoelectron angular distribution of multiphoton ionization of CO_2 in strong laser fields, Phys. Rev. A **80**, 011403(R) (2009).

[76] B. Zhang, J. Yuan, and Z. Zhao, Dynamic core polarization in strong-field ionization of CO molecules, Phys. Rev. Lett. **111**, 163001 (2013).

[77] V. P. Majety and A. Scrinzi, Dynamic exchange in the strong field ionization of molecules, Phys. Rev. Lett. **115**, 103002 (2015).

[78] S. Ohmura, H. Ohmura, T. Kato, and K. H., Manipulation of multielectron dynamics of molecules by fourier-synthesized intense laser pulses: Effective potential analysis of CO, Front. Phys. **9**, 677671 (2021).

[79] M. D. Śpiewanowski and L. B. Madsen, Alignment- and orientation-dependent strong-field ionization of molecules: Field-induced orbital distortion effects, Phys. Rev. A **91**, 043406 (2015).

[80] V. H. Trinh, V. N. T. Pham, O. I. Tolstikhin, and T. Morishita, Weak-field asymptotic theory of tunneling ionization including the first-order correction terms: Application to molecules, Phys. Rev. A **91**, 063410 (2015).

[81] H. Nakamura, *Nonadiabatic Transition: Concepts, Basic Theories and Applications* (World Scientific, New Jersey, 2012).

[82] *NIST Chemistry WebBook, NIST Standard Reference Database Number 69*, edited by P. J. Linstrom and W. G. Mallard (National Institute of Standards and Technology, Gaithersburg, MD, 2024).

[83] G. Nemeth, H. Selzle, and E. Schlag, Magnetic ZEKE experiments with mass analysis, Chem. Phys. Lett. **215**, 151 (1993).

[84] L. Klasinc, Application of photoelectron spectroscopy to biologically active molecules and their constituent parts: III. Amino acids, J. Electron Spectrosc. Relat. Phenom. **8**, 161 (1976).

[85] A. Landers, T. Weber, I. Ali, A. Cassimi, M. Hattass, O. Jagutzki, A. Nauert, T. Osipov, A. Staudte, M. H. Prior, H. Schmidt-Böcking, C. L. Cocke, and R. Dörner, Photoelectron diffraction mapping: Molecules illuminated from within, Phys. Rev. Lett. **87**, 013002 (2001).